PAPER

Check for updates

Engineering nitrogen doping of silicon oxycarbide structures through tailored dendritic molecular architectures

Berta Pérez-Román, (ID) *[ab] M. Alejandra Mazo, (ID) [a] Alejandro Merchán del Real,[c] Juan Rubio[a] and Fernando Rubio-Marcos (ID) *[a]

Polymer-derived ceramics, such as silicon oxycarbide (SiOC) materials, offer broad tunability through precursor chemistry, enabling the development of multifunctional materials. Controlling nitrogen incorporation into SiOC systems remains a key challenge to tailor their structure and properties. Here, we show that the design of dendritic molecules with triazine and amine functionalities, allows effective nitrogen doping of SiOC materials. Polymerization with allyl-hydrido polycarbosilane at controlled temperatures, followed by pyrolysis from 700 to 900 °C, leads to the integration of nitrogen both into the free-carbon phase as pyridinic-N, graphitic-N, and pyrrolic-N species, and into the glassy network through Si–N bonds. Materials polymerized at 50 °C exhibit enhanced nitrogen retention in the form of graphitic-N and greater cross-linking. This work demonstrates a molecular-level strategy to control nitrogen doping in SiOC ceramics, paving the way for the design of functional materials for advanced applications such as catalysis, energy storage, and sensing, which will be tested in future works.

1. Introduction

In the ongoing effort for the synthesis of advanced ceramic materials with superior properties, the polymer-derived ceramic (PDC) route[1] is proving to be an effective method, enabling facile strategies to obtain Si-based ternary and quaternary ceramics. PDCs have gained significant interest due to their unique properties such as thermal stability, high elastic modulus, corrosion and oxidation resistance, and chemical stability. In addition to their functional properties and promising microstructures, PDCs have been extensively studied for a wide range of potential applications, including their use in supercapacitor electrodes,[2,3] anodes for lithium-ion batteries,[4–6] pressure sensors,[7,8] high-temperature applications,[9,10] and scenarios requiring high oxidation and corrosion resistance.[11,12]

Silicon oxycarbides (SiOC) and silicon carbonitrides (SiCN) are among the most extensively studied PDCs. They can be produced from different polymeric precursors, undergoing a controlled pyrolysis of organosilicon-based polymers. The ceramic networks of SiOC and SiCN are constituted by varied tetrahedral

units, SiC_xO_{4-x}, and SiC_xN_{4-x}, respectively, along with a free carbon phase (C_{free}), or the so-called segregated carbon.[13] The amount of C_{free} and its crystallinity and microstructure have been shown to significantly influence the final properties of the PDCs. A high content of segregated carbon can be detrimental for the mechanical performance or high-temperature applications of the PDC materials. Conversely, several authors have described the benefits of the C_{free} phase in the structural and functional properties of the PDCs, such as enhanced electrical[14,15] and electrochemical performance,[2] and/or corrosion resistance.[11] Additionally, numerous studies have highlighted the importance of the molecular architecture of the starting polymeric precursor, directly affecting the final ceramic structures and their evolution through the polymer-to-ceramic transformation.[16–19] This unique characteristic of PDCs allows the precise tailoring of the final ceramic structures through the molecular design of the initial starting precursor, allowing precise structural control. Consequently, current research focuses on obtaining carbon-enriched PDCs[20] and improving their functional properties by effectively incorporating heteroatoms into both, the glassy matrix and the C_{free} phase. Different processing routes are being explored to promote the doping of boron[21,22] and/or nitrogen[23,24] heteroatoms.

N-doped SiOC has attracted particular attention due to its ability to modulate the nature of bonding and the distribution of nitrogen species within the C_{free} and the SiOC glassy phase. This enables the design of tailored materials for specific applications. N-doping can be strategically performed to

[a] Instituto de Cerámica y Vidrio (ICV-CSIC), C/Kelsen 5, 28049 Madrid, Spain. E-mail: berta.perez@icv.csic.es, frmarcos@icv.csic.es; Fax: +34 91 735 58 43; Tel: +34 91 735 58 40

[b] Escuela de Doctorado UAM, Francisco Tomás y Valiente 2, 28049 Madrid, Spain

[c] Departamento de Química Orgánica, Facultad de ciencias, Universidad Autónoma de Madrid, C/Francisco Tomás y Valiente. 7, 28049 Madrid, Spain

introduce heteroatoms in different bonding configurations, such as pyridinic-N, graphitic-N, pyrrolic-N or N-oxide.[25] Numerous studies have reported that high concentrations of pyridinic nitrogen are well-suited for electrocatalytic applications,[26,27] whereas those with highly concentrated graphitic nitrogen are desirable for electronic and energy storage devices.[28] This tunability makes N-doped SiOC materials highly desirable for cutting-edge technological applications.

In our previous work,[29] a well-defined processing route to synthesize N-doped SiOC was established from an allyl-hydrido polycarbosilane (AHPCS) and a novel N-containing dendritic molecule. The polymerization and the subsequent thermal treatment of the AHPCS and the dendron resulted in the formation of SiOCN structures, where N was presented both in the SiOC network and in the carbonaceous phase. To go further into this investigation, two new dendritic molecules with superior complexity, elevated nitrogen concentrations and distinct nitrogen functionalities, were designed to evaluate their influence on the nitrogen doping and to achieve effective structural control of these SiOC-based ceramic structures.

In this study, an effective route for the development of N-doped SiOC materials is proposed through the tailored design of N-containing dendritic molecules. The influence of the N bonding in the starting dendritic structures is demonstrated, as well as the control of the synthesis route for effective nitrogen retention in the final materials. The optimization of the processing route was carried out by carefully investigating the three sequential steps involved in the synthesis procedure: (a) design and synthesis of novel N-containing dendritic molecules, (b) cross-linking of the dendrons with a commercially available AHPCS to promote the chemical modification of this polymer, and the addition of the N atoms into the AHPCS structure, and finally, (c) the polymer-to-ceramic transformation promoted by pyrolysis treatment for obtaining N-doped SiOC materials.

2. Experimental section

2.1 Synthesis of dendritic molecules

Two novel dendritic molecules are designed and synthesized with different active centers and varied vinyl groups, with the latter placed at the terminal positions of the dendrons, to enhance the reactivity for further polymerization with the commercial AHPCS. These newly synthesized dendrons are named as PIP-2 (or D2) and TREN-3 (or D3), where "PIP" and "TREN" represent the chemical structures selected for the active centers (*i.e.* piperazine and tris-aminoethylamine, respectively), and the number signifies the amount of chemical substitutions involved in the synthesis of each dendritic molecule. The synthesis procedures of PIP-2 and TREN-3 are outlined as follows, and the synthetic protocol and molecules under investigation are depicted in Fig. 1.

To synthesize PIP-2 and TREN-3 dendrons, it is imperative to create a new molecule to promote substitution reactions with the corresponding active centers. Regarding the synthesis of the TRIAZ-3 dendron presented in our previous work,[29] an intermediate product obtained after di-substitution was prepared and used as a precursor for the synthesis of PIP-2 and TREN-3 dendrons. This intermediate precursor molecule is named TRIAZ-2, according to the name assignment described previously.

2.1.1 Synthesis of intermediate TRIAZ-2: 6-chloro-N^2,N^4-bis(4-vinyl phenyl)-1,3,5-triazine-2,4-diamine. The synthesis of TRIAZ-2 was performed using cyanuric chloride ($C_3N_3Cl_3$) and N,N-diisopropylethylamine (DIPEA), both obtained from Sigma-Aldrich (USA), along with 4-vinylaniline (90%) from Fisher Scientific (USA), and anhydrous toluene (99.8%). The reaction progress was monitored by thin layer chromatography (TLC) employing F_{254} aluminium oxide plates. To ensure the purification of the product, column chromatography was employed using silica gel 60 (60–120 mesh) as the stationary phase (Merck, USA). It is noteworthy that the chemicals were used as received without any additional purification. The synthesis commenced with the dissolution of 16 g (0.086 mol) of $C_3N_3Cl_3$ and 35 mL (0.2 mol) of DIPEA in 250 mL of anhydrous toluene. The mixture was stirred at room temperature (RT) and purged with argon to establish an inert atmosphere during the chemical reaction. Thereafter, 30.18 mL (0.258 mol) of 4-vinylaniline was added dropwise, and the reaction mixture was then heated under reflux for 8 h. The final residue was purified by column chromatography with 1:4 ethyl acetate/hexane as the eluent, yielding a white solid product (>85% yield).

2.1.2 Synthesis of PIP-2 (D2): 6,6′-(piperazine-1,4-diyl)bis-(N^2,N^4-bis(4-vinyl phenyl)-1,3,5-triazine-2,4-diamine. PIP-2 was
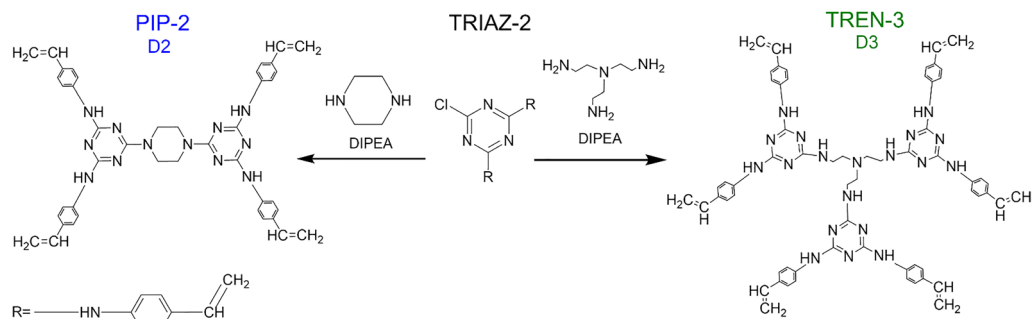
Fig. 1 Synthetic pathway for the preparation of PIP-2 (D2) and TREN-3 (D3) dendrons from the intermediate molecule TRIAZ-2. Note that TRIAZ-2 molecule was used to promote the substitution reactions of the amine groups of both, piperazine and tris-amino-ethylamine in the presence of DIPEA. Both reactions were conducted at the corresponding temperature and for the reaction times described in the text.

synthesized by the dissolution of 4 mL (0.023 mol) of DIPEA and 688 mg (0.008 mol) of piperazine (Sigma-Aldrich, USA) in 250 mL of anhydrous tetrahydrofuran (THF). The molecule TRIAZ-2 (5.5 g, 0.016 mol) was then added into the solution, previously dissolved in anhydrous THF. The reaction mixture was stirred, bubbled with argon and sealed in a Parr's vessel to remove the oxygen content. The mixture was then heated at 80 °C for 12 h, and the progress of the reaction was monitored by TLC. The anhydrous THF was then removed using a rotatory evaporator and the final residue was purified by column chromatography with 5 : 1 dichloromethane/methanol as the eluent, thus obtaining a final white residue (>85% yield).

2.1.3 Synthesis of TREN-3 (D3): N^2-(2-(bis(2-((4,6-bis((4-vinyl phenyl) amino)-1,3,5-triazine-2-yl)amino)ethyl)-N^4,N^6-bis(4-vinyl phenyl)-1,3,5-triazine-2,4,6-triamine. The synthesis of TREN-3 was accomplished through the dissolution of 6.95 mL (0.04 mol) of DIPEA and 1.168 g (0.008 mol) of tris(2-aminoethyl)amine (Sigma-Aldrich, USA) in 250 mL of anhydrous THF. Subsequently, 10 g (0.028 mol) of TRIAZ-2 was dissolved in anhydrous THF and added into the aforementioned solution, and the resulting mixture was stirred, bubbled with argon and sealed in a Parr's vessel to remove the oxygen content. The mixture was then heated at 80 °C for 14 h until complete consumption of TRIAZ-2 was observed by TLC. Upon completion of the reaction, the THF was removed using a rotatory evaporator, and the final residue was obtained by washing the solid with ethyl acetate and acetone, yielding a yellowish solid (>90% yield).

2.2 Synthesis of N-doped silicon-based ceramic materials

A commercially available AHPCS (SMP-10®, Starfire Systems, USA) was employed to obtain a silicon-based ceramic material, while D2 and D3 contributed to the N-doping of the structure, resulting in the formation of SiOCN structures. Materials were prepared from a mixture of the AHPCS used as received and the corresponding D2 and D3 dendrons at a ratio of 90 : 10 wt/wt, respectively. The chemical reactions were conducted on a Schlenk line using anhydrous THF as a solvent and in the presence of 1 wt% of the Pt-based catalyst (platinum-1,3-divinyl-1,1,3,3-tetramethyldisiloxane (3–3.5% Pt), abcr GmbH, Germany). The mixtures were thoroughly stirred under an argon atmosphere, and two distinct polymerization conditions were examined for each precursor. Polymerization was conducted at (i) RT for 48 h and (ii) at 50 °C, fixing the reaction time according to the concentration of vinyl groups on each dendritic molecule. Thus, the reaction at 50 °C lasted 48 h for the D2 dendron, while it lasted 24 h when D3 was involved. After the completion of the chemical reactions, the solvent was removed under reduced pressure, yielding yellowish gummy materials. To streamline the sample labelling, the materials were categorized into four distinct series: D2RT, D3RT, D25C, and D35C. The prefixes "D2" and "D3" denote the dendrons employed for nitrogen doping, while "RT" indicates polymerization conducted at room temperature, and "5C" refers to materials synthesized through reactions carried out at 50 °C.

After polymerization, materials were heated to 280 °C for 5 h at a rate of 5 °C min^{-1} to promote the crosslinking of the AHPCS with the dendrons, thereby ensuring optimum bonding between both structures. This was followed by pyrolysis at 700, 800 and 900 °C for 2 h. The obtained SiOCN samples were named according to the criteria described previously, with 7, 8 or 9 at the end to denote the pyrolysis temperature employed (700, 800 or 900 °C). The final materials were ground in an agate mortar, following by sieving to obtain particles smaller than 45 μm. This procedure was conducted prior to the extensive characterization of the ceramic structures.

2.3 Characterization techniques

The characterization of the organic molecules (D2 and D3) involved liquid-state nuclear magnetic resonance (NMR) spectroscopy and mass spectrometry (MS), both of which were used to elucidate the chemical structures of the synthesized molecules and their respective molecular weights. The NMR study was conducted on a Bruker Avance Neo (USA) instrument by diluting the samples in dimethyl sulfoxide (DMSO) and recording ^{1}H (500 MHz), ^{13}C (125 MHz) and ^{13}C NMR distortionless enhancement by polarization transfer 135° (DEPT-135) analyses. Conventional notation was employed, where dd means doublet of doublet and s-br means broad singlet. J is defined as the coupling constant associated with the *cis*, *trans* or *geminal* position of alkenyl hydrogens (J_{cis}, J_{trans} and J_{gem}). In addition, J is also defined as the coupling constant associated with the *ortho*, *meta* and *para* positions of aromatic hydrogens (J_{ortho}, J_{meta} and J_{para}). The MS analysis was conducted by diluting the samples in methanol, and using an Agilent 6520 Accurate-Mass LC/MS Q-TOF (USA).

The starting precursors and the evolution of the obtained polymeric structures were investigated through attenuated total reflectance Fourier transform infrared spectroscopy (ATR-FTIR). A PerkinElmer BX (USA) spectrophotometer, equipped with an ATR device and a diamond crystal plate, was employed for the analysis, averaging over at least 32 scans per sample. Thermogravimetry and differential thermal analysis (TG-DTA) were used to study the thermal behavior of the starting samples and the different preceramic materials using an SDT Q600 TA instrument (USA). The measurements were performed by heating the samples under an argon flow of 100 cm^3 min^{-1} up to 1000 °C at a heating rate of 10 °C min^{-1}.

The composition of N-doped SiOC materials was analysed using quantitative elemental analysis of carbon, nitrogen and oxygen concentrations. Analyses were performed using Leco (USA) CS-200 and RC-412 analyzers, while silicon content was calculated by difference. Structural investigations were conducted by FTIR in a PerkinElmer BX spectrophotometer (USA) using KBr pellets prepared with the powders, averaging over at least 32 scans per sample. The solid-state NMR technique was conducted to study the structural units of SiOCN materials using a Bruker (USA) AV-400-WB device with a 4 mm probe head. ^{29}Si was studied by magic-angle spinning (MAS) and ^{13}C nuclei by high-power decoupling magic-angle spinning (HPDEC-MAS). These experiments were performed by direct

irradiation with a frequency of 100.61 MHz, $\pi/3$ pulse length at 65 kHz, and a relaxation time of 20 seconds. The carbonaceous phase was investigated by Raman spectroscopy using a Renishaw inVia spectrophotometer (UK) with an Ar^+ ion laser with an excitation wavelength of 514 nm. Spectra were recorded with an accumulation time of 10 s and an accumulated signal from 10 scans.

X-ray photoelectron spectroscopy (XPS) was used to examine the surface composition of the prepared materials, employing a SPECS GmbH (Germany) apparatus, equipped with an ultra-high vacuum system and an energy analyser (PHOIBOS 150 9MCD). Non-monochromatic Mg radiation was employed as the energy source (200 W and 12 kV), with a sampling area of $500 \times 500\ \mu m^2$. All the spectra were calibrated based on the peak position of C 1s (284.6 eV), and a Shirley background correction was applied by using the CASA XPS software. Finally, microstructural characterization was performed by field emission scanning electron microscopy (FE-SEM) investigations using a Hitachi S-4700 (Japan) microscope. Except for gold sputtering of the powders, no other preparation for the FE-SEM examination was performed.

3. Results and discussion

3.1 Characterization of dendritic structures

A thorough characterization of D2 and D3 dendrons was conducted to verify their intended chemical structures. This study also encompassed the exploration of their structural and microstructural features and morphology. The investigations

of these novel dendrons commenced with their structural determination using NMR and MS techniques to ascertain the molecular structures. The results of these analyses are displayed in the SI, displaying the NMR spectra of both dendrons (see Fig. S1–S6, Section S1, SI), including ^1H, ^{13}C and ^{13}C DEPT-135 spectra.

The ^1H NMR spectrum of the D2 dendron is shown in Fig. S1 (SI), and the following information is provided. δ_H (ppm): H1 (3.9 (sbr, 8H)), H2 (5.16 (d, J_{cis} = 10.99 Hz, 4H)), H3 ((5.74 (d, J_{trans} = 17.68 Hz, 4H)), H4 (6.70 (dd, J_{trans} = 17.60 Hz and J_{cis} = 10.93 Hz, 4H)), H5 (7.42 (d, J_{ortho} = 8.31 Hz, 8H)), H6 (7.78 (d, J_{ortho} = 8.15 Hz, 8H)) and H7 (9.3 (sbr, 4H)). The ^{13}C NMR elucidates the following carbon resonances δ_C (ppm) (Fig. S2, SI): C1 (43.19), C2 (112.48), C3 (120.30), C4 (126.81), C5 (131.28), C6 (136.86), C7 (140.39), C8 (164.48) and C9 (165.12). The ^{13}C NMR DEPT-135 (Fig. S3, SI) δ_C (ppm) data corroborate the following assignments: C1 (43.19, CH_2), C2 (112.48, CH_2), C3 (120.30, CH), C4 (126.81, CH) and C6 (136.86, CH). Within the domain of the MS and through the measurement of the mass-to-charge ratio of the ions, the molecular mass was verified, finding 357.18 m/z $[M + 2H]^{2+}$ and 713.356 $[M + H]^+$, and it was ascertained that D2 structure corresponds to $C_{42}H_{40}N_{12}$ and 712.35 g mol^{-1}.

D3 dendron was characterized by the following ^1H NMR δ_H (ppm) values, as illustrated in Fig. S4 (SI): H1 (2.82 (d, J = 7.33 Hz, 6H), H2 (3.51 (d, J = 8.70 Hz, 6H)), H3 (5.12 (d, J_{cis} = 10.93 Hz, 6H)), H4 (5.69 (d, J_{trans} = 17.63 Hz, 6H)), H5 (6.67 (dd, J_{trans} = 17.60 Hz and J_{cis} = 10.93 Hz, 6H)), H6 (7.36 (d, J_{ortho} = 8.35 Hz, 12H)), H7 (7.80 (d, J_{ortho} = 8.26 Hz, 12H)), H8 (9.09 (sbr, 3H)), and H9 (9.18 (sbr, 6H)). ^{13}C NMR (Fig. S5, SI) δ_C (ppm): C1
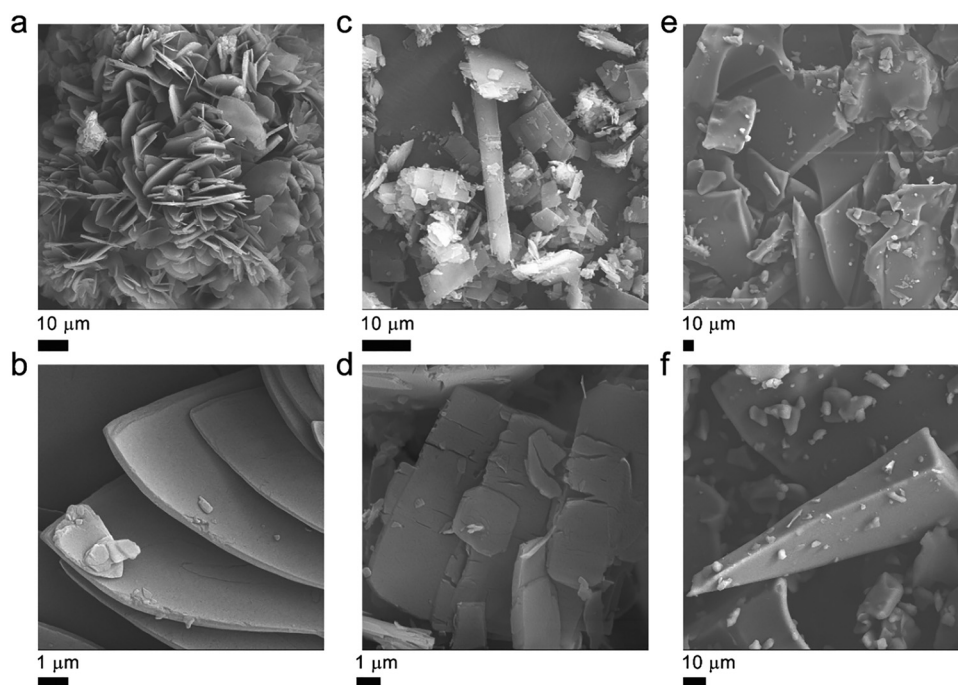

Fig. 2 Microstructural examination of the different N-containing dendritic molecules. Micrographs obtained by FE-SEM at different magnification levels. (a), (b) TRIAZ-2 molecule; (c), (d) D2 and (e), (f) D3 dendrons.

(39.25), C2 (54.27), C3 (112.21), C4 (120.15), C5 (126.67), C6 (131.06), C7 (136.89), C8 (140.67), C9 (164.56) and C10 (166.21). The ^{13}C NMR DEPT-135 (Fig. S6, SI) δ_C (ppm) data corroborate the following assignments: C1 (39.25, CH$_2$), C2 (54.27, CH$_2$), C3 (112.21, CH$_2$), C4 (120.15, CH), C5 (126.67, CH) and C7 (136.85, CH), MS: calculated for C$_{63}$H$_{63}$N$_{19}$: 1085 g mol^{-1}, found: 543.78 m/z [M + 2H]$^{2+}$ and 1086.56 [M + H]$^+$.

FE-SEM was utilized to examine the morphology of the as-prepared dendritic molecules, thereby unveiling the distinctly divergent microstructures of both, the TRIAZ-2 precursor and the synthesized D2 and D3 dendrons. The obtained micrographs are shown in Fig. 2. The TRIAZ-2 molecule manifests as flower-like platelet aggregates (Fig. 2a), exhibiting variations in size. Upon closer inspection (Fig. 2b) of some of the "leaves" within the microstructures, uniform thicknesses with dimensions of less than a micron are observed. In contrast, the D2 dendron manifests as a rectangular platelet shape with similar thicknesses below 500 nm (Fig. 2c and d), while D3's microstructure is based on irregular polygonal particles with greater thicknesses, up to 10 μm (Fig. 2e and f). The microstructural design of the dendritic structures was accomplished by varying both, the structural complexity and the molecular weight, thereby resulting in distinct microstructures of each novel molecule, as illustrated in Fig. 2. Furthermore, nitrogen atoms were strategically positioned at diverse chemical sites, encompassing N-sp^2 hybridization within the triazine compounds, and N-sp^3 hybridization within the piperazine and the amine-based active center.

In this investigation, a particular emphasis is placed on the role of the different N configurations, elucidating the influence of the initial architecture of the dendron molecules towards the nitrogen doping of Si(O)C-based materials. Additionally, the influence of the processing conditions on promoting diverse nitrogen bonding configurations throughout the SiOCN processing route was also examined.

3.2 Characterization of the chemically modified preceramic polymeric precursor

### 3.2.1 Crosslinking between AHPCS and N-containing dendrons.
Following the synthesis of the novel dendritic structures, polymerization reactions were conducted to promote the bonding between dendrons and the commercial AHPCS employing the reaction parameters described previously. In this section, materials were examined by IR spectroscopy in two distinct states: firstly, upon completion of the chemical reaction, and subsequently, following the cross-linking process performed at the start of the pyrolysis treatments, which entails the heating of the samples at 280 °C for 5 h.

Fig. 3 shows the FTIR spectra of unmodified D2 and D3 dendrons, and as-received AHPCS. Characteristic AHPCS bands are reported elsewhere.[29] Si–H groups (934 and 2120 cm^{-1}) participate in hydrosilylation with dendron vinyl groups and in self-cross-linking via allyl groups (1631 and 3076 cm^{-1}), while Si–CH$_2$–Si (1036 cm^{-1}) and Si–C (750 and 832 cm^{-1}) bonds[21,30] remain unaffected (Fig. 3a). The spectra of D2 and D3 display multiple absorption bands at low to medium wavenumbers, with several common features. N–H linkages in D2 are identified by bands at 1567, 3270, and 3404 cm^{-1}, corresponding to bending, symmetric, and asymmetric stretching modes, respectively[31,32] (Fig. 3a and b). Aromatic rings are detected by a C–H stretching band at 3083 cm^{-1}, while vinyl groups show C–H vibrations in the range 2800–3100 cm^{-1} and a conjugated C=C vibration at 1631 cm^{-1}. The breathing mode of triazine rings is observed at 836 cm^{-1}, labelled as *t in Fig. 3b, along with C–N (1219, 1305, 1401, and 1487 cm^{-1}) and C=N (1487 and 1624 cm^{-1}) stretching vibrations.[33–35]

Distinctive features differentiate the dendrons. In D2, the breathing mode of the piperazine ring appears at 1005 cm^{-1}, denoted as *p in Fig. 3b, with additional CH$_2$ rocking and twisting vibrations at 1084 and 1263 cm^{-1}, respectively.[36,37] In D3, besides the N–H bond between triazine and aromatic units, a new N–H band emerges at 1568 cm^{-1}, attributed to the bonding between the triazine and tris-aminoethylamine active center.[38]

Then, the spectra of materials derived from the D2 dendron (D2RT and D25C) are presented in Fig. 4, both after the completion of the chemical reactions and subsequent to the cross-linking treatment, while the spectra of AHPCS, D3RT and D35C samples are displayed in Fig. S7 (Section S2, SI). Bonding between AHPCS and triazine dendrons occurs mainly through hydrosilylation between Si–H and vinyl groups,[29] with Si–N
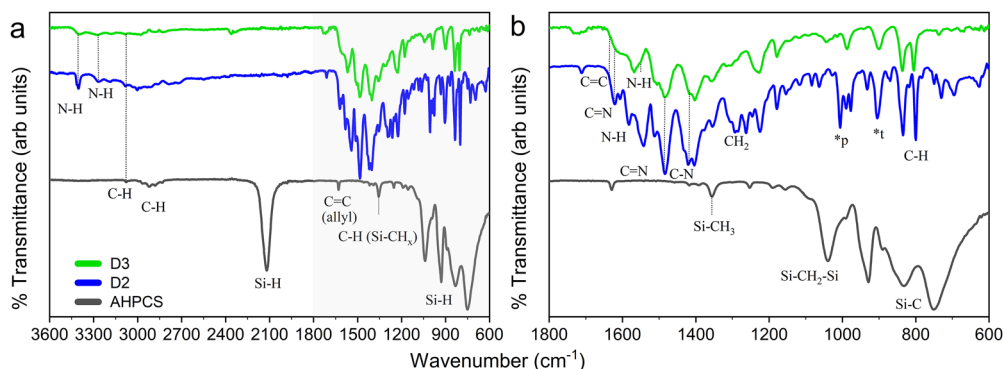
Fig. 3 Structural information of the starting precursors through FTIR spectroscopy. IR spectra of AHPCS and the as-synthesized D2 and D3 dendrons in different spectral ranges: (a) 3600–600 and (b) 1800–600 cm^{-1}. This plot illustrates the initial molecular structures of the starting precursors, discerning the representative chemical groups of the novel dendrons.
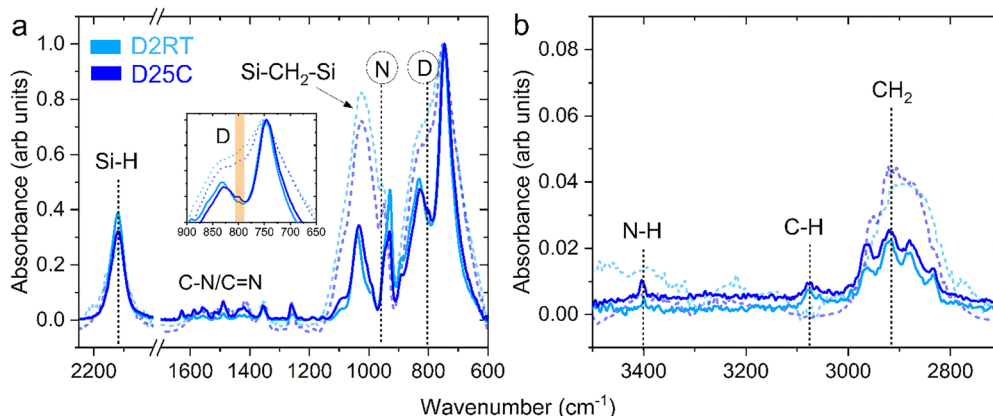
Fig. 4 Investigations of the thermally assisted cross-linking mechanism. Normalized IR spectra of materials prepared from the D2 dendron (D2RT and D25C samples) in the (a) 2250–600 and (b) 3500–2700 cm^{-1} spectral ranges, showing the structural evolution of materials before and after completion of the cross-linking stage performed at 280 °C for 5 h. (Note that cross-linked materials are shown by short dotted lines.)

bonds forming after dendron fragmentation upon heating. In Fig. 4 and Fig. S7 (SI), characteristic vibrations of both AHPCS and dendrons are present, although dendron signals are weaker due to their low concentration. The preservation of C–N, C=N, and N–H vibrations indicates that the dendrons maintain their chemical integrity after polymerization. A new band appears around 800 cm^{-1}, labelled as D (Fig. 4a and Fig. S7a, SI), along with a decrease in the Si–H bands (2120 cm^{-1}), confirming the formation of Si–CH$_2$–CH$_2$–C bonds.[29] The D

band shows greater intensity in D25C and D35C, suggesting that polymerization at 50 °C enhances the bonding between AHPCS and dendrons (see Fig. 4a and Fig. S7c of the SI).

Cross-linking (dotted lines in the spectra) follows two mechanisms: (i) free-radical-induced cross-linking *via* allyl group cleavage[39] and (ii) hydrosilylation and dehydrocoupling reactions between allyl and Si–H groups.[40] These processes are evidenced by the disappearance of allyl-related bands (1630 and 3080 cm^{-1}), a reduction in Si–H bands (929 and 2120 cm^{-1}),
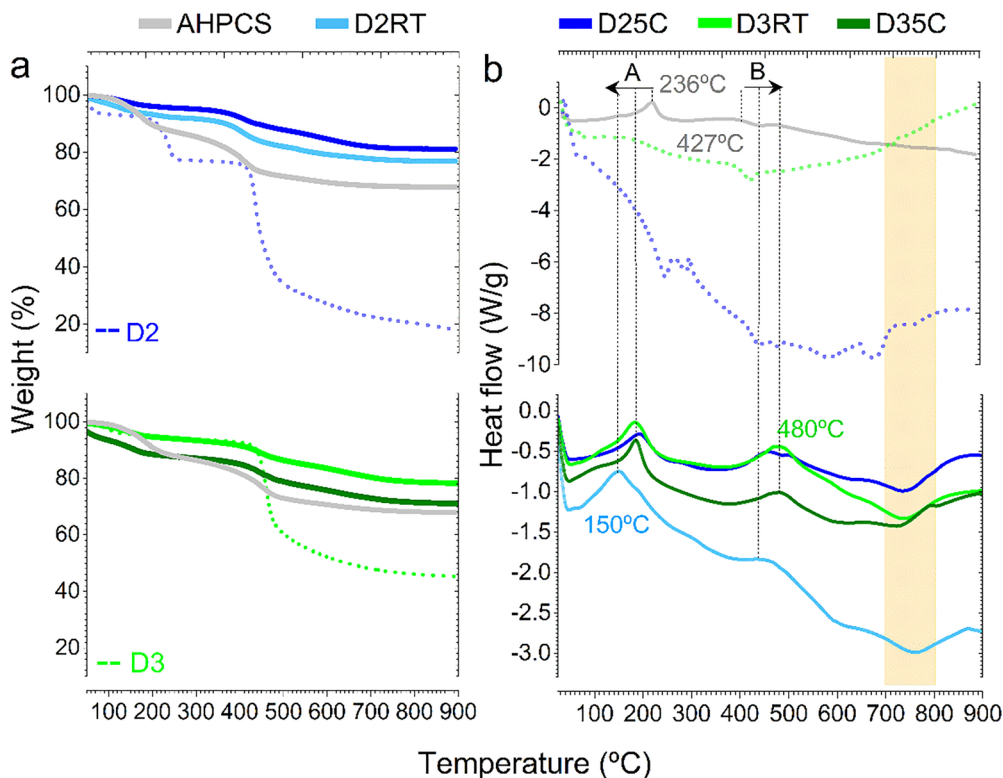

Fig. 5 Study of the influence of dendron introduction into the polymer-to-ceramic transformation. (a) TG analysis of materials prepared from D2 and D3 dendrons with varying synthesis parameters (dendritic structures are shown with short dotted lines). (b) DTA curves of the starting precursors (AHPCS and dendrons (D2 and D3)) (top plot), and the prepared materials (bottom plot) highlighting the shift of the characteristic peaks.

and an increase in –CH$_2$– bands (2914 cm^{-1}) (Fig. 4b and Fig. S7b, SI).[30,41,42] The D band at $\sim$800 cm^{-1} intensifies after cross-linking, with unexpectedly higher intensity in D2RT (Fig. 4a), which was analyzed later *via* thermal analysis (Fig. 5).

Compared to AHPCS (Fig. S7a and b), dendron-containing materials exhibit stronger reductions in Si–H bands and enhanced formation of CH$_2$ groups (2914 and 1036 cm^{-1}), suggesting a higher cross-linking degree. In addition, a new peak appears at $\sim$945 cm^{-1}, referring to N (Fig. 4a and Fig. S7c SI), while the N–H band at 3404 cm^{-1} disappears. This suggests Si–N bond formation through the fragmentation of D2 and D3 dendrons during cross-linking and subsequent reaction with Si–H bonds. While dendron degradation was previously observed after pyrolysis,[29] the present results show that partial dendron degradation has already started during cross-linking at temperatures below 280 °C, facilitating the incorporation of N within the preceramic matrix.

3.2.2 Polymer-to-ceramic conversion. Upon completion of the polymerization reactions conducted at RT and 50 °C, the thermal behavior of the prepared materials was investigated by TG-DTA measurements. As explained previously, two reaction pathways compete during the initial stage of thermal treatment: the crosslinking of the AHPCS with itself and the polymerization with each respective dendritic molecule. As illustrated in Fig. 5a and b, the TG-DTA analysis of the initial materials (AHPCS, D2 and D3) and the resulting reaction products (D2RT, D3RT, D25C and D35C) was conducted.

The TG curve of AHPCS shows three weight losses between 50–300 °C, 300–600 °C, and 600–1000 °C (Fig. 5a). The first stage corresponds to cross-linking reactions, with an exothermic peak at 236 °C (denoted as peak A in Fig. 5b), associated with the removal of low molecular weight oligomers. Above 300 °C, H$_2$ release occurs, related to dehydrocoupling and redistribution reactions of Si–H/Si–C bonds. In addition, above 600 °C, ceramization reactions take place, leading to the formation of an amorphous Si(O)C network, in agreement with the XRD patterns displayed in Fig. S8 (Section S3, SI).[39]

The TG curves of the D2 and D3 dendrons show weight losses at 480 °C and 460 °C, respectively, with associated endothermic peaks (Fig. 5a). Solvent release is detected up to 120 °C, originating from trapped solvents during synthesis or purification. D2 displays an additional weight loss at 261 °C, attributed to partial dendron fragmentation.

In polymerized materials (Fig. 5b), peak A shifts to lower temperatures compared to AHPCS, indicating that dendron incorporation facilitates cross-linking, in agreement with ATR-FTIR results (Fig. 4 and Fig. S7, SI). D25C, D3RT, and D35C show peak A around 185 °C, while D2RT shifts further to $\sim$150 °C. This greater shift in D2RT correlates with the higher intensity of FTIR bands at 800, 950, and 1036 cm^{-1} (Fig. 4), indicating enhanced cross-linking after the 280 °C treatment. This behavior also reflects the thermal profile of D2, suggesting partial degradation during prolonged polymerization at 50 °C, whereas polymerization at RT preserves the dendritic structure. These results demonstrate that dendron incorporation increases the cross-linking degree of AHPCS, facilitating the

cross-linking reactions. Similar catalytic effects have been reported by Wilhelm *et al.*[43] using nickel acetylacetonate, and by Ionescu *et al.*[44] using tetrakis(dimethylamido)hafnium(IV) (TDMAH), both accelerating hydrosilylation and dehydrocoupling reactions.

At higher temperatures, the peak around 427 °C (denoted as peak B in Fig. 5b) associated with redistribution reactions, shifts to higher values upon dendron incorporation. D2RT and D25C exhibit peak B at $\sim$458 °C, while in D3RT and D35C it shifts it to $\sim$480 °C, reflecting the higher structural complexity of the D3 dendron, which hinders redistribution processes. This shift indicates increased network complexity and difficulty in bond rearrangement during polymer-to-ceramic transformation. Finally, a new peak appears around 740 °C (highlighted region in Fig. 5b), attributed to the release of residual species following the initial stages of ceramization.

3.3 Characterization of the ceramic material

3.3.1 Microstructural analysis of the pyrolyzed materials. The materials were examined using FE-SEM to explore the different microstructural features developed through the polymer-to-ceramic transformation, as well as the effects induced by the introduction of the dendritic molecules. The microstructures of 2RT7, 25C9 (Fig. 6a and b) and 3RT7, 35C9 (Fig. 6c and d) are shown, representing the extremes of the processing conditions (*i.e.* crosslinking at RT followed by pyrolysis at 700 °C, and polymerization at 50 °C followed by thermal treatment at 900 °C).

The different micrographs shown in Fig. 6 display irregular-shaped particles of similar sizes in materials prepared with either D2 or D3 dendrons. These particles feature sharp edges, which become more prominent as the pyrolysis temperatures increase, indicating a further progress from the polymer to the ceramic state. Moreover, comparing the materials prepared with each dendritic molecule, distinct features are clearly observed in D2 and D3 dendron-derived samples. The latter exhibit planar particles devoid of visible porous or surface defects, while materials prepared using the D2 dendron display highly defective and inhomogeneous surface particles. These microstructural defects/inhomogeneities are likely associated with the introduction of this dendritic molecule, as they are clearly visible in materials prepared under extreme synthesis condition: 2RT7 and 25C9 materials (Fig. 6a and b). This phenomenon can be tentatively associated with the dual thermal profile of the D2 dendron, which has been shown to induce significant fracture of the dendritic structure, resulting in surface defects/inhomogeneities in the final materials.

3.3.2 Study of the elemental composition. After polymerization of AHPCS with D2 and D3 dendrons, materials were pyrolyzed, yielding ceramic structures with distinct compositions analyzed by elemental analysis (Table 1). The materials pyrolyzed at higher temperatures show an increased C content and a decreased O concentration. The maximum C contents are observed in D25C9 and D35C9 samples, reaching 33.6 wt% and 34.35 wt%, respectively. The reduction in O content at elevated
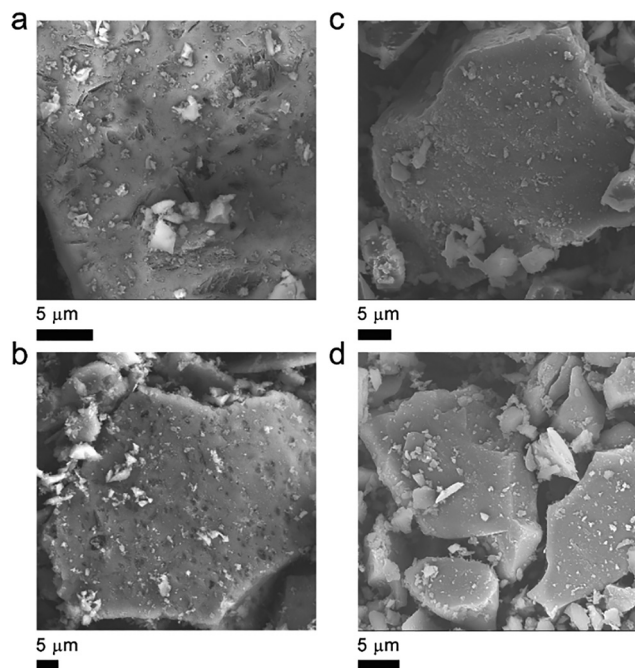
Fig. 6 Surface morphology analysis of the pyrolyzed materials. FE-SEM micrographs of the materials prepared using D2 and D3 dendrons under different synthesis conditions (crosslinking at RT with subsequent pyrolysis at 700 °C, and polymerization at 50 °C followed by thermal treatment at 900 °C): (a) 2RT7, (b) 25C9, (c) 3RT7 and (d) 35C9 materials.

temperatures is attributed to the lower oxygen uptake during bond rearrangement and ceramization reactions.[39]

Comparatively, materials obtained after chemical reactions at RT or 50 °C display a variation in the O percentage (%O). D25C and D35C samples show lower %O values, indicating that higher polymerization degrees, promoted by temperature, hinder oxygen capture. This behavior is consistent with ATR-FTIR and TG-DTA analyses (see Fig. 4, 5 and Fig. S7, SI), which show an enhanced cross-linking structure preventing oxygen incorporation. Regarding nitrogen content, establishing a clear relationship with synthesis parameters is challenging. In addition, no significant differences are detected between D2- and

D3-derived materials in terms of final nitrogen concentration, which are in the range of 1.4–2 wt%, aligning with the similar nitrogen heteroatom content of the initial dendrons. In a previous study[29] using a simpler molecular dendron, limited nitrogen incorporation was reached. Thus, the present results suggest that the novel D2 and D3 dendritic structures enable more efficient nitrogen doping into the ceramic network, enhancing the overall integration of nitrogen species during the polymer-to-ceramic transformation.

3.3.3 Structural analysis using the FTIR technique. Following elemental analysis, the FTIR technique was employed to elucidate the molecular structures of the pyrolyzed materials, and to assess the influence of the dendritic molecules and thermal treatment.

Fig. 7a shows the FTIR spectra of the prepared samples. Two prominent bands are detected in all spectra, centred at approximately 790 cm^{-1} and 1000 cm^{-1}, corresponding to the vibrations of Si–C and Si–CH$_2$–Si bonds, respectively.[29] An evolution of the band located at 1000 cm^{-1} is observed with increasing temperature, with a progressive reduction in intensity relative to the band at 790 cm^{-1}, indicating the elimination of Si–CH$_2$–Si units and the concomitant formation of SiC$_4$ units,[44] thus promoting the three-dimensional network typical of SiC precursors.[29]

To further investigate the structural features, a Gaussian deconvolution of the FTIR spectra between 1300 and 400 cm^{-1} was performed. Fig. 7b presents the fitted spectra for D3RT7 and D25C9 samples, with the deconvolution data summarized in Table S1 (Section S2, SI). Besides the fundamental Si–C vibrations and the medium-intensity band at ~620 cm^{-1}, attributed to the AHPCS precursor,[29] a new band emerges at ~940 cm^{-1} in all samples, referred to as the Si–N bond formation signature, previously identified in the crosslinked materials (Fig. 4a and Fig. S7c, SI). The intensity of this Si–N band shows a slight increase in materials treated at 900 °C (Table S1, SI), suggesting enhanced formation of Si–N linkages at elevated temperatures, likely due to the greater integration of dendritic structures with AHPCS. Additional signals characteristic of Si–O bonds are observed: low-intensity bands around

Table 1 Compositional analysis of SiOCN prepared by different temperature treatments. The data were obtained from the elemental analysis of materials prepared by polymerization reactions (RT and 50 °C) and temperature pyrolysis (700, 800 and 900 °C). The concentration of each element was used for the calculation of the empirical formula (note: silicon was calculated by difference)

| Sample	Weight %				Empirical formula
	Si	O	C	N	
D2RT7	55.46	14.60 ± 0.20	27.85 ± 0.05	1.73 ± 0.22	SiO$_{0.46}$C$_{1.17}$N$_{0.06}$
D2RT8	57.88	9.48 ± 0.13	30.75 ± 0.05	1.62 ± 0.25	SiO$_{0.29}$C$_{1.23}$N$_{0.06}$
D2RT9	58.23	8.81 ± 0.02	31.35 ± 0.15	1.68 ± 0.07	SiO$_{0.27}$C$_{1.26}$N$_{0.06}$
D25C7	56.78	11.22 ± 0.18	30.45 ± 0.05	1.35 ± 0.07	SiO$_{0.35}$C$_{1.25}$N$_{0.05}$
D25C8	58.53	8.65 ± 0.03	31.00 ± 0.10	1.87 ± 0.02	SiO$_{0.26}$C$_{1.23}$N$_{0.06}$
D25C9	57.79	7.16 ± 0.04	33.60 ± 0.30	2.00 ± 0.20	SiO$_{0.22}$C$_{1.37}$N$_{0.07}$
D3RT7	53.27	14.95 ± 0.25	29.35 ± 0.25	1.77 ± 0.18	SiO$_{0.49}$C$_{1.27}$N$_{0.07}$
D3RT8	56.95	10.50 ± 0.10	30.80 ± 0.20	1.95 ± 0.04	SiO$_{0.32}$C$_{1.27}$N$_{0.07}$
D3RT9	56.96	8.57 ± 0.08	32.40 ± 0.10	1.71 ± 0.17	SiO$_{0.26}$C$_{1.33}$N$_{0.06}$
D35C7	58.44	11.65 ± 0.25	28.60 ± 0.20	1.35 ± 0.14	SiO$_{0.35}$C$_{1.14}$N$_{0.05}$
D35C8	56.23	12.45 ± 0.15	29.70 ± 0.20	1.87 ± 0.02	SiO$_{0.39}$C$_{1.24}$N$_{0.07}$
D35C9	55.39	8.75 ± 0.15	34.35 ± 0.15	1.70 ± 0.02	SiO$_{0.28}$C$_{1.45}$N$_{0.06}$
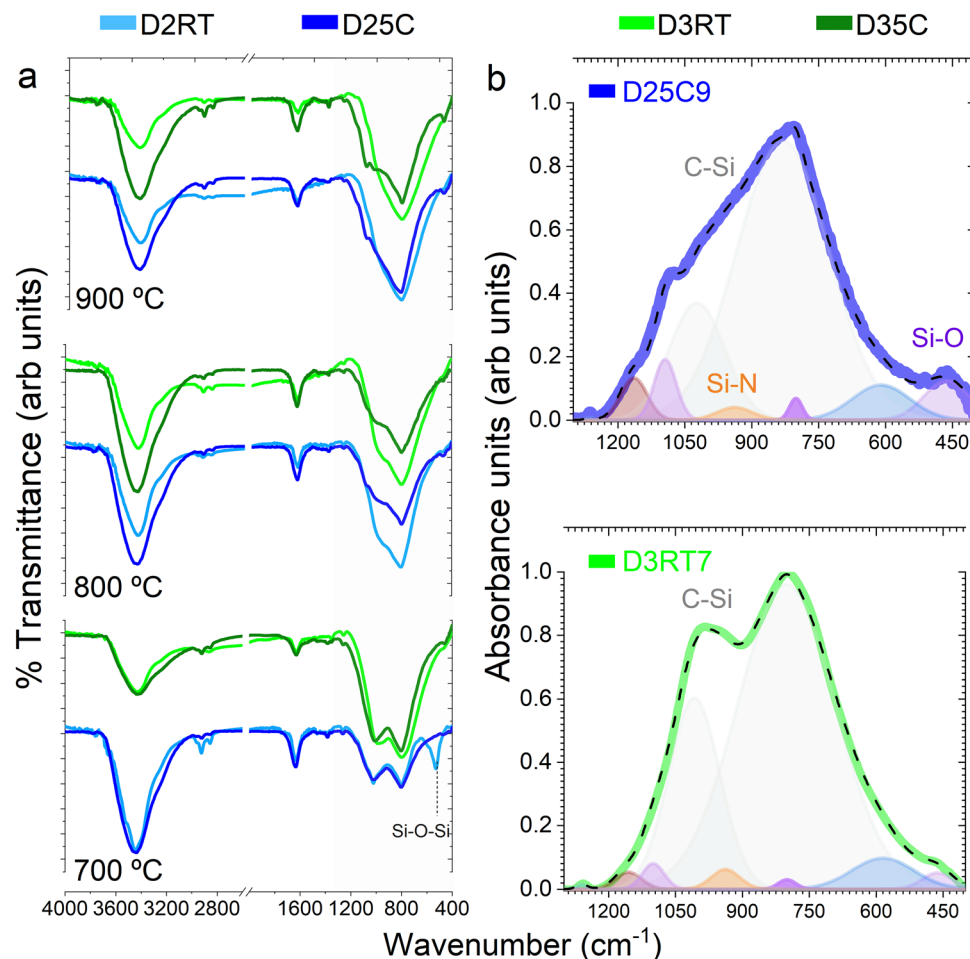
Fig. 7 Structural evolution elucidated by IR spectroscopy of materials treated at 700–900 °C. (a) FTIR curves of the pyrolyzed materials as a function of pyrolysis temperature and discerning materials prepared at RT and 50 °C. (b) Deconvolution of D25C9 and D3RT7 samples in the spectral range of 1300–400 cm^{-1}.

465 cm^{-1} and 800 cm^{-1}, associated with the bending and symmetric stretching vibrations of Si–O, respectively, indicative of SiO$_4$ units. Moreover, bands positioned around 1100 and 1160 cm^{-1} are identified, corresponding to Si–O–Si asymmetric stretching vibrations.[45]

In the D2RT7 sample, a distinct band appears around 525 cm^{-1} (Fig. 7a), attributed to Si–O–Si bending vibrations, along with a higher intensity band at ~1110 cm^{-1}, assigned to Si–O–Si asymmetric stretching.[46] These observations suggest enhanced oxidation reactivity, consistent with the highest oxygen content found by elemental analysis (Table 1). This indicates that polymerization at RT followed by thermal treatment at 700 °C favors the formation of silica-like phases. By contrast, D25C and D35C materials exhibit heightened intensities at 1164, 1095, 800, and 465 cm^{-1}, indicating an increased formation of Si–O bonds. This behavior can be attributed to the presence of silica phases or oxygen-enriched SiC$_x$O$_{4-x}$ structural units. The phenomenon is particularly pronounced in the D25C9 material (see Fig. 7b). Considering the low oxygen contents detected (Table 1), the enhanced band intensities are tentatively assigned to the formation of SiC$_x$O$_{4-x}$ phases rather than pure silica domains.

3.3.4 Insights into the N doping in SiOCN materials *via* XPS analysis. XPS analysis was employed to investigate the surface composition and electronic states (C 1s, O 1s, N 1s, and Si 2p) of the pyrolyzed materials, with a focus on the bonding configurations of N atoms. Table 2 summarizes the survey elemental composition (wt%) of the SiOCN samples, showing slight variations relative to the bulk elemental analysis (see also Table 1). This phenomenon is reported previously[29] and attributed to minor surface oxidation of the SiOC-based materials. Thus, the nitrogen concentrations obtained by XPS, ranging from 1.6 to 2.2 wt%, align closely with the bulk values, confirming a high degree of consistency between surface and bulk measurements.

The bonding environments are elucidated through pseudo-Gaussian deconvolution of the high-resolution spectra. Assuming proportionality between the area under each component and the abundance of the corresponding chemical bond, XPS allows assessment of the relative concentrations of the different N species. The N 1s high-resolution spectra of the initial D2 and D3 dendrons (Fig. S9, Section S4, SI) reveal two contributions centred at 398.3 eV and 399.7 eV, attributed to C=N bonds

**Table 2** Surface elemental composition obtained from the XPS survey spectra of the various SiOCN materials

Sample	Surface elemental composition (wt%)				Sample				
	Si	O	C	N		Si	O	C	N
D2RT7	52.5	17.5	27.9	2.2	D3RT7	52.5	17.8	27.8	1.9
D2RT8	51.8	20.6	25.7	2.0	D3RT8	51.9	20.1	26.4	1.6
D2RT9	51.7	21.3	25.0	2.0	D3RT9	52.0	21.2	25.0	1.8
D25C7	51.4	19.7	26.7	2.2	D35C7	51.8	19.6	26.9	1.7
D25C8	51.1	21.7	25.2	2.0	D35C8	51.1	21.2	25.7	2.0
D25C9	51.6	21.5	25.0	1.9	D35C9	50.7	22.7	24.8	1.8

within triazine rings (pyridinic-N) and C–NH–C sp³ bonds (amine-N), respectively.[47]

The N 1s XPS spectra of the SiOCN materials are displayed in Fig. 8, where four distinct contributions are identified at around 397.0, 398.3, 399.5, and 401.0 eV. The band placed at 397.0 eV is attributed to N–Si bonds, evidencing the reaction between AHPCS and the dendritic structures, in agreement with the FTIR results (Fig. 7). Notably, in samples pyrolyzed at 900 °C, the main N 1s peak shifts towards lower binding energies, indicating a greater incorporation of N into the ceramic network *via* N–Si bonds at higher temperatures (Table 3). This suggests that elevated pyrolysis temperatures favor dendron fragmentation and N–Si bond formation. The materials polymerized at RT exhibit higher N–Si concentrations, particularly for the D2 dendron, pointing to enhanced dendron fragmentation in less cross-linked structures compared to those obtained at 50 °C. This observation is consistent with the stronger FTIR Si–N signature detected in the pyrolyzed materials (see Table S1, SI).

The contribution at 398.3 eV is denoted as pyridinic-N,[48] confirming the retention of triazine rings from the initial dendritic structures. The dominant intensity of this peak suggests that nitrogen heteroatoms predominantly adopt pyridinic configurations, located at vacancies or edges of carbon domains.[49] The contributions located at 399.5 eV and 401.0 eV are assigned to pyrrolic-N and graphitic-N species, respectively.[50,51] The formation of pyrrolic-N is attributed to cross-linking and bond rearrangement processes during the polymer-to-ceramic transformation, involving H loss and dendron rupture, particularly from the cleavage of amine-N bonds.[29] The resulting fragments can undergo intramolecular cyclization with alkene (C=C) groups, leading to pyrrolic nitrogen structures.[52] The presence of graphitic-N is tentatively ascribed to the bonding of triazine rings with C_{free} phase, facilitating the incorporation of nitrogen atoms into the hexagonal carbon framework.

It is evident that D25C and D35C materials exhibit an increased intensity of the band positioned around 401 eV, indicative of the formation of a higher amount of graphitic-N arising from the bonding of AHPCS with the dendritic molecules at 50 °C. This phenomenon is particularly pronounced in D35C samples, where the relative concentration of graphitic-N reaches up to 39%. This enhanced graphitic-N formation could be tentatively associated with the higher amine-N content in the initial D3 dendron, suggesting that amine groups contribute to the reactivity of the dendritic structures by virtue of their ability
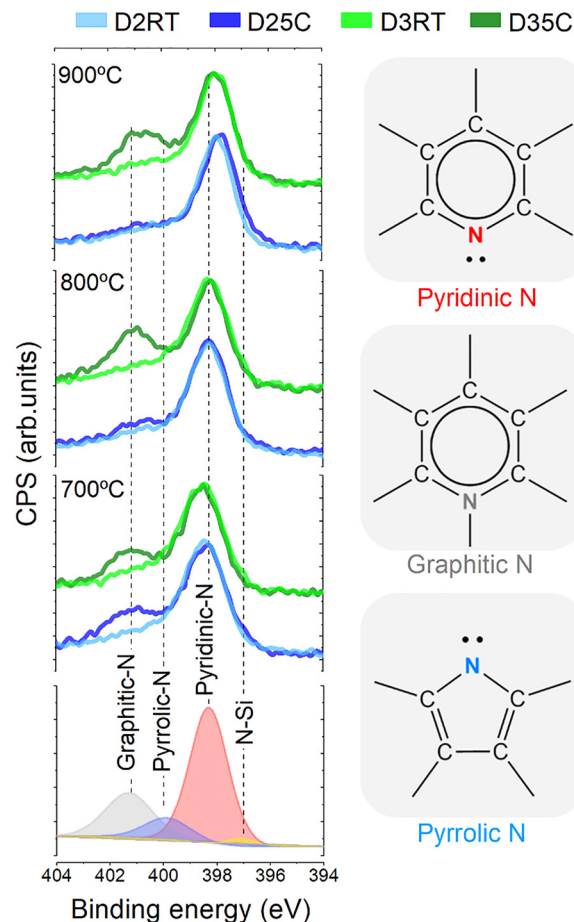
Fig. 8 High-resolution N 1s XPS spectra of the pyrolyzed materials and their corresponding pseudo-Gaussian deconvolution. This plot highlights the varied nitrogen configurations introduced into the pyrolyzed materials, namely pyridinic-N, graphitic-N and pyrrolic-N, which coexist with N–Si bonds established in the glassy phase.

to donate electron pairs, thereby promoting various chemical reactions.[53,54] The high-resolution C 1s spectra of the SiOCN materials, illustrated in Fig. 9a, were subjected to pseudo-Gaussian deconvolution, yielding five distinct peaks. The detailed deconvolutions of materials prepared from D2 and D3 dendrons are provided in Tables S2 and S3 (Section S4, SI). Unlike our previous study,[29] where four peaks were identified with a single contribution for carbon–carbon bonds centered at 285.1 eV (C=C sp²), in this study, the C=C sp² and C–C sp³ contributions were distinguished, with the latter attributed to defective carbon structures.[55] Consequently, the C 1s spectra feature five components centered at 283.5, 284.6, 285.6, 287.3, and 288.8 eV, corresponding to C–Si, C=C (sp²), C–C (sp³), C–N, and C–O/=O bonds, respectively.[56,57] The presence of a representative C–N related band across all samples further evidences nitrogen incorporation into the C_{free} phase, in agreement with the N 1s XPS spectra (Fig. 8). Larger relative concentrations of C–N bonds are observed for D25C and D35C materials (Tables S2 and S3, SI), confirming a slightly increased nitrogen incorporation under polymerization at 50 °C, consistent with the trend observed in the N 1s spectra. A ratio between the relative

Table 3 Relative concentrations (%) of the different N functionalities (pyridinic-N, pyrrolic-N, graphitic-N and N–Si bonds) presented in the pyrolyzed materials, discerned from the high-resolution N 1s spectra

| Sample	Relative concentration of N functionalities (%)				Sample				
	Pyridinic-N	Pyrrolic-N	Graphitic-N	N–Si		Pyridinic-N	Pyrrolic-N	Graphitic-N	N–Si
D2RT7	67.2	10.5	9.5	12.9	D3RT7	60.7	18.6	15.0	5.7
D2RT8	59.1	14.7	16.4	14.7	D3RT8	77.1	5.8	13.7	3.4
D2RT9	52.5	17.1	11.0	19.7	D3RT9	70.0	12.1	15.2	2.7
D25C7	60.7	9.7	26.4	3.2	D35C7	65.6	14.5	18.7	1.2
D25C8	66.4	12.8	17.5	3.3	D35C8	47.3	8.0	39.1	5.0
D25C9	72.1	10.8	14.1	2.9	D35C9	51.2	7.3	35.1	6.4

concentrations of C–C sp^3 and C=C sp^2 is established (C sp^3/C sp^2), in order to illustrate the increased order degree with temperature pyrolysis (Table S2, SI). Additionally, a progressive increase in the formation of C–Si bonds is detected with higher pyrolysis temperatures, as reflected by the enhanced intensity of the peak at 283.5 eV in materials treated from 700 to 900 °C (Tables S2 and S3, SI). This trend suggests increased formation of Si–C linkages associated with the polymer-to-ceramic transformation promoted at elevated temperatures.

The high-resolution Si 2p XPS spectra and their corresponding pseudo-Gaussian fittings are shown in Fig. 9b and summarized in Table S4 (Section S4, SI), revealing four distinct

Fig. 9 Surface analysis by means of XPS: (a) C 1s and (b) Si 2p XPS spectra of the different sets of pyrolyzed materials between 700 and 900 °C, and their corresponding fitting by pseudo-Gaussian deconvolution.

contributions located at approximately 101.2, 102.2, 103.2, and 104.7 eV. These are assigned to the Si–C bonds in SiC$_x$O$_{4-x}$ units (SiC$_4$), the Si–N and Si–O bonds in SiC$_x$O$_{4-x}$ units, and the Si–O bonds in SiO$_4$ units, respectively. Among them, the band at 101.2 eV appears as the most intense across all materials, indicative of a dominant presence of Si–C bonds within the SiC$_x$O$_{4-x}$ structural framework. A progressive shift of this peak towards lower binding energies with increasing pyrolysis temperature suggests a greater transformation towards SiC$_4$ structures, as previously reported,[39] and is in line with the formation of new Si–C linkages between AHPCS and dendrons within SiO(C) structures.[29] The band at around 102.2 eV corresponds to the Si–N bonds formed between AHPCS and the dendritic structures, corroborating the observations from FTIR analysis (Fig. 7). Moreover, an asymmetry towards higher binding energies is observed in materials polymerized at 50 °C, particularly in D35C samples, becoming more pronounced with increasing pyrolysis temperature. This asymmetry is attributed to a slight increase in the intensity of the Si–O peak within the SiC$_x$O$_{4-x}$ units, reaching maximum prominence in the D35C9 material. The deconvolution results for materials prepared from the D3 dendron, presented in Table S4 (Section S4, SI), highlight more pronounced changes in the spectra (Fig. 9b), suggesting a slightly enhanced detection of SiC$_x$O$_{4-x}$ units at the surface, in agreement with the higher surface oxygen content revealed in Table 2.

3.3.5 Study of the structural units by means of ^{29}Si and ^{13}C NMR. Following the evaluation of the fundamental bonding environments within the SiOCN materials, ^{29}Si and ^{13}C MAS NMR analyses were carried out to explore silicon coordination and carbon speciation. The corresponding spectra are shown in Fig. 10a and b. As reported in our previous study,[29] the ^{29}Si NMR spectra of the N-doped samples exhibit a prominent peak centered around −6 ppm, displaying a downfield shift of approximately 4 ppm as the pyrolysis temperature increases from 700 to 900 °C. Notably, the polymerization temperature also influences the NMR response: samples polymerized at 50 °C show a clear shift compared to those polymerized at room temperature, particularly at lower pyrolysis temperatures (700 °C) (Fig. 10a). The broadness of the NMR signals points to the coexistence of several silicon-based structural environments. Through Gaussian deconvolution, three main contributions were identified, located at around 10, −8, and −20 ppm (Table S5, Section S5, SI). The first two bands correspond to SiC$_3$O and SiC$_4$ units, respectively, with the SiC$_4$ signal being
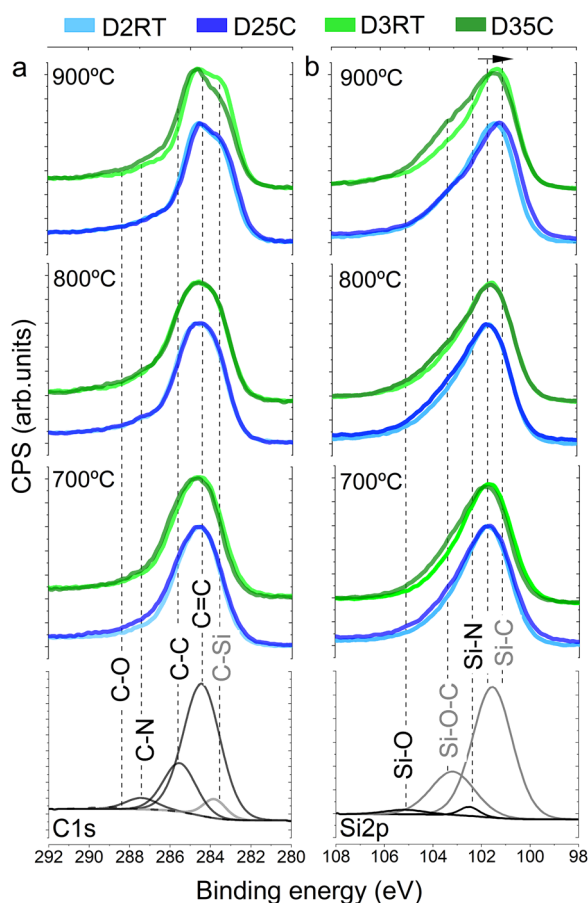
Paper
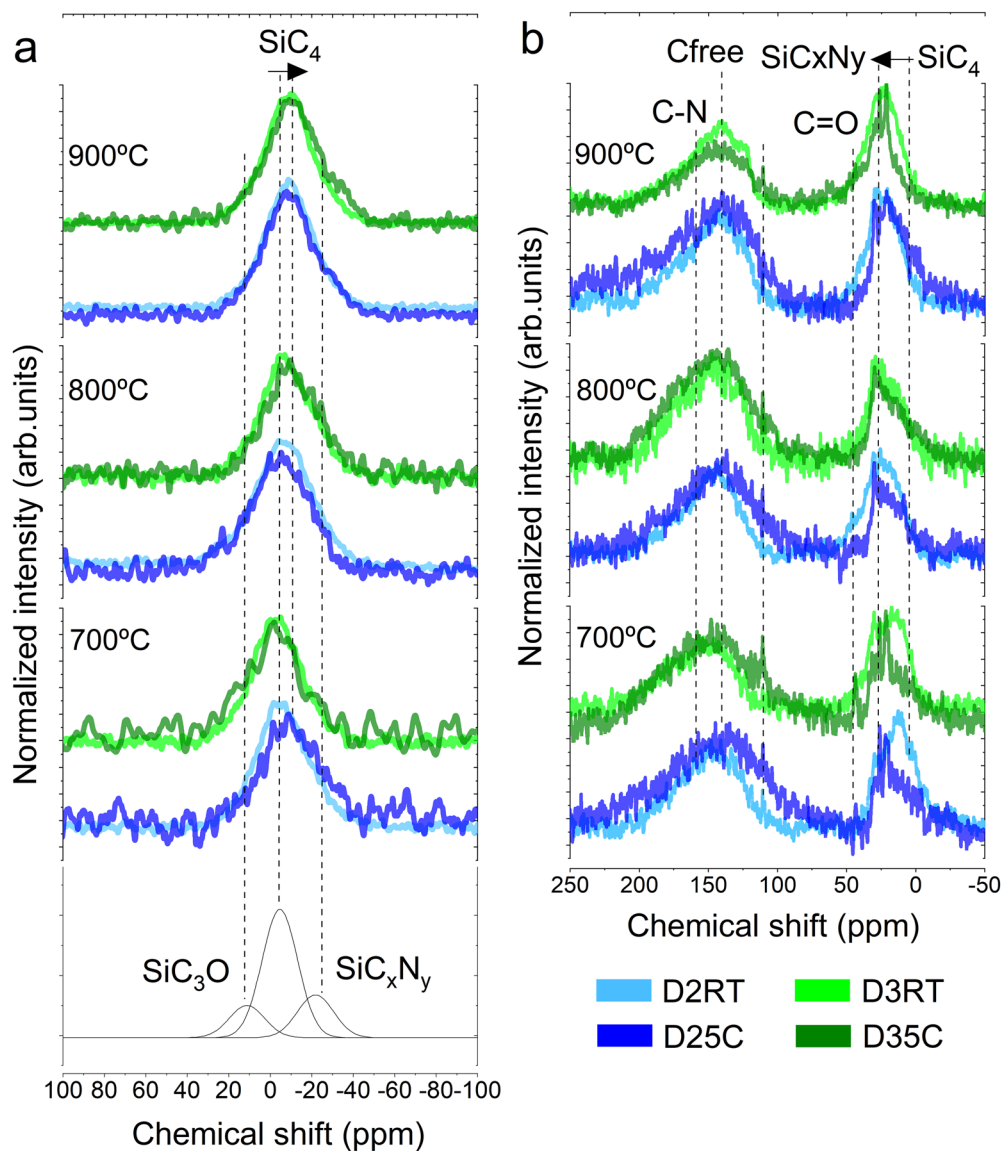
Fig. 10 Elucidation of the different structural units by NMR studies: (a) ^{29}Si-MAS NMR, and (b) ^{13}C-MAS NMR. Materials prepared by D2 and D3 incorporation are shown in blue and green colours, respectively. Samples obtained by polymerization reactions conducted at RT and 50 °C are displayed in light and dark colours, respectively.

the most intense and slightly increasing in relative proportion at higher pyrolysis temperatures, consistent with the increased formation of more fully carbide units. A third contribution around −22 ppm is observed and tentatively attributed to SiC_2N_2 units, although these species are not typically expected under these pyrolysis conditions.[39] The asymmetry of the main peak, extending toward more negative chemical shifts, suggests the presence of Si–N containing species (SiC_nN_{4-n} units), as previously indicated by the FTIR (Fig. 7) and XPS results (Fig. 8 and 9). In particular, Bahloul *et al.*[58] assigned chemical shifts at −10, −19, and −34 ppm to SiC_3N, SiC_2N_2, and $SiCN_3$ units, respectively, allowing us to tentatively associate the observed band near −20 ppm with the SiC_2N_2 environment. Interestingly, the materials synthesized from the D3 dendron at 50 °C exhibit higher fractions of these Si–N containing units

compared to their counterparts polymerized at RT (Table S5, Section S5, SI), suggesting a greater incorporation of nitrogen into the Si–C framework under these conditions. No significant signals were detected at −110 or −50 ppm, corresponding to SiO_4 or SiN_4 units,[59] respectively. This indicates that the oxygen content reported in Table 1 is primarily integrated as SiC_xO_{4-x} units, with additional C–O bonds likely arising from minor surface oxidation, as supported by XPS (Fig. 9a). Likewise, the lack of SiN_4 signals (Fig. 10a) further supports the conclusion that nitrogen incorporation occurs mainly through the formation of SiCN units, contributing to the development of a partially N-doped glassy network.

As shown in Fig. 10b, the ^{13}C-NMR spectra of the prepared materials reveal two broad signals centered around ~15 ppm and 135 ppm, corresponding to sp^3-hybridized carbon (carbon

bonded to silicon in SiCO or SiCN units) and sp^2-hybridized C_{free}, respectively. The broadness of both bands reflects the low crystallinity degree of the SiOCN materials, indicating a highly disordered structure for both the carbon-rich phase and the carbon bonded to silicon. The overlapping nature of these signals points to the coexistence of multiple types of carbon bonds within the materials. A closer look at Fig. 10b shows a clear evolution of the asymmetry of the peak located between 0 and 50 ppm, particularly noticeable when comparing samples pyrolyzed at 700 °C to those treated at higher temperatures. This effect is particularly pronounced in the D2RT and D3RT series. Typically, the Si–C (sp^3) bonds in SiOC structures appear at chemical shifts below ∼30 ppm, while the N–C (sp^3) bonds in SiCN moieties tend to shift upfield, appearing above 30 ppm.[58] Within this context, the increased signal intensity around 21 ppm is assigned to SiC_4 species, whereas the pronounced asymmetry observed in samples polymerized at 50 °C suggests a higher presence of SiCN units. This finding aligns well with the increased detection of SiC_2N_2 environments previously identified by ^{29}Si-NMR (see Fig. 10a). In the range from 100 to 200 ppm, the spectra capture resonances from sp^2-hybridized carbon atoms, with the disordered C_{free} phase typically appearing as a broad signal between 120 and 140 ppm.[60] The width of this band further highlights the amorphous character of the carbonaceous domains. Moreover, the noticeable asymmetry of the sp^2 region suggests the incorporation of nitrogen-substituted aromatic structures—such as pyridine-like, graphitic-N, or pyrrolic-like units—as supported by the XPS findings (Fig. 8). These N functionalities exhibit downfield shifts in δ relative to C_{free}, displaying signals in the range of 150–190 ppm,[61] which provides direct evidence for nitrogen doping within the carbonaceous network.

**3.3.6 Carbonaceous phase analysis by Raman spectroscopy.** The Raman spectra of the pyrolyzed materials are presented in Fig. 11a and b, excluding the samples treated at 700 °C due to strong fluorescence effects. All analyzed materials display two main bands, characteristic of carbon-based systems: the D and G bands, located at around 1350 and 1570 cm^{-1}, respectively.

The D band is linked to lattice disorder and corresponds to the A_{1g} vibration mode, reflecting structural defects in graphitic carbon. In contrast, the G band arises from the E_{2g} phonon mode of sp^2 carbon atoms and serves as an indicator of the graphitic order and crystallinity of the carbon phases.[62,63] The Raman spectra reveal a significant overlap between the D and G bands, a typical feature influenced by the pyrolysis temperature during the polymer-to-ceramic transformation.[13] However, a noticeable reduction in this overlap is observed in materials treated at 900 °C, particularly those derived from the D2 dendron. Clear differences in the relative intensities of the bands between the materials treated at 800 and 900 °C, point towards a decrease in the degree of order of the carbon phase at higher temperatures.

To better quantify the disorder, the I_D/I_G ratio was determined through Gaussian deconvolution (see Table S6 in Section S6 of the SI), and the lateral size (L_a) of the carbon clusters was calculated using the correlation proposed by Ferrari et al.[64] A slight increase in the I_D/I_G ratio is observed with increasing pyrolysis temperature, especially in materials prepared by polymerization at 50 °C, reflecting the growth of the disordered C_{free} phase, typically expected at this low pyrolysis temperature, where the phase separation has not commenced yet. Its formation occurs within the Si(O)C network and high local strains are generated over the graphene layers increasing the disorder as the pyrolysis temperature increases.[65] The L_a values remain relatively consistent across the samples, with a slight increase observed for D2-derived materials and as the pyrolysis temperature increases, ranging from 1.4 to 1.6 nm. As reported in our previous study,[29] the deconvolution was refined by including two additional bands centered around 1190 and 1460 cm^{-1}, referred to as D* and D″, respectively (Fig. 11c). The D* band is associated with impurities disrupting the graphite layer stacking, while D″ is related to amorphous carbon species involving both sp^2 and sp^3 hybridizations.[56] Importantly, the D* band is considered a signature of nitrogen doping,[66] reinforcing the nitrogen incorporation into the SiOC structures detected by XPS (Fig. 8). Regarding the second-order Raman region, signals corresponding to the overtone of the D band (G′ at ∼2700 cm^{-1})
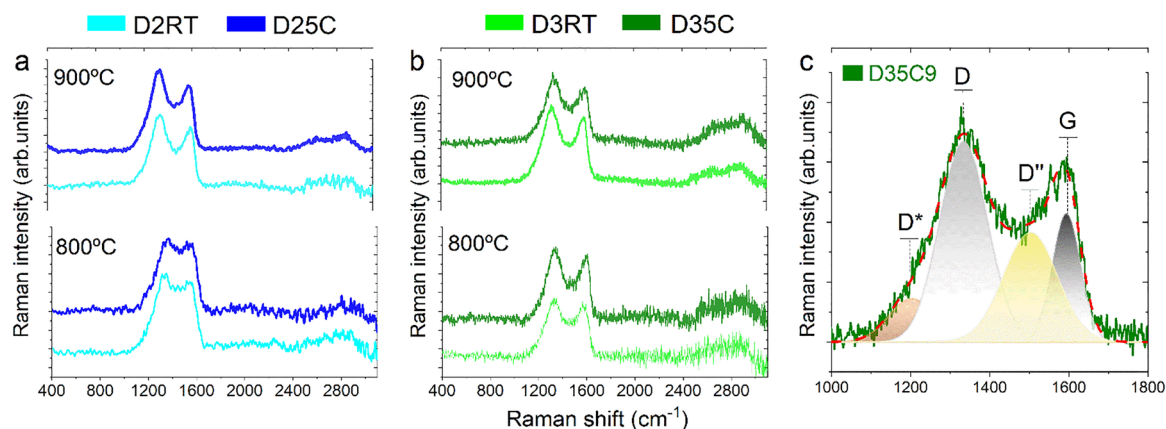
Fig. 11 Analysis of the carbonaceous phase by Raman spectroscopy. Raman spectra of the prepared materials by the incorporation of (a) D2 (blue), and (b) D3 (green) dendrons at 800 °C and 900 °C. Note that materials treated at 700 °C are not included due to the fluorescence phenomenon. (c) Characteristic deconvolution performed over the Raman spectrum of D35C9.
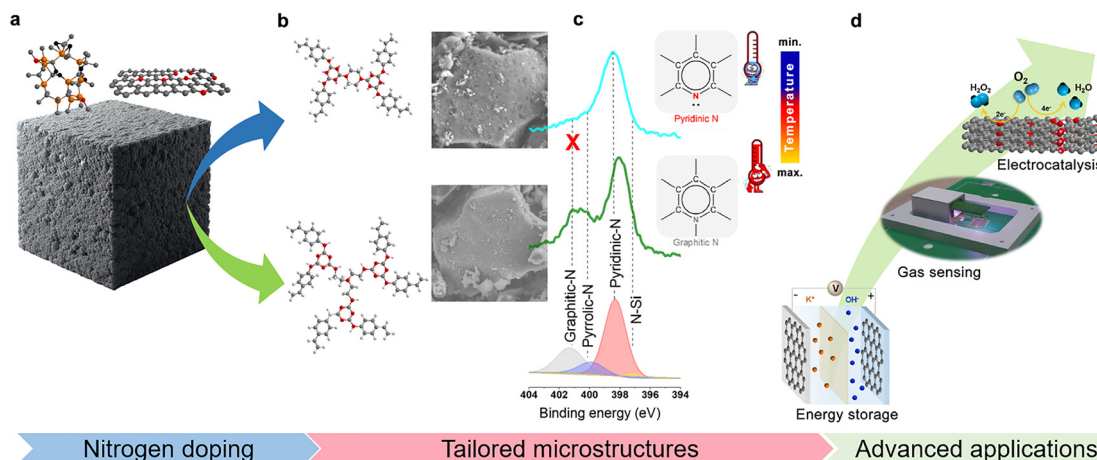
Fig. 12 Potential of dendritic structures for engineered ceramic processing. This figure highlights the potential of novel dendron molecules for nitrogen doping in ceramic materials, opening new possibilities for advanced applications. (a) N-doped SiOC structures with nitrogen incorporated in both the glassy phase and the C_{free} phase. (b) Microstructural design of ceramic materials to control surface defect concentration. (c) Influence of temperature on nitrogen doping. (d) Potential advanced functional applications of the prepared materials.

and the D + G combination band $(\sim 2920 \text{ cm}^{-1})$, typically indicative of highly graphitic materials,[67,68] are not clearly distinguished due to the high signal-to-noise ratio.

In summary, our results underline the potential of dendritic architectures and controlled thermal treatments to tailor the microstructure and properties of nitrogen-doped SiOC materials. Dendron-based strategies promote effective nitrogen incorporation into both the glassy and C_{free} phases fundamentally as pyridinic-N and graphitic-N (Fig. 12a), which are highly demanded for cutting-edge applications. The modulation of N functionalities is achieved both by the rational design of the dendritic structures based on N–C sp^2 and N–C sp^3,[69] and by adjusting the synthesis parameters during processing. While the D2 dendron favors increased surface roughness and defect density, the D3 dendron promotes less-defective frameworks (Fig. 12b). Polymerization at 50 °C significantly enhances cross-linking, leading to better structural integration and higher retention of nitrogen, particularly as graphitic-N species (Fig. 12c). These findings pave the way for future applications in catalysis, energy storage, and sensing technologies (Fig. 12d), emphasizing the value of exploring dendritic design and synthesis optimization to develop next-generation functional ceramics.

4. Conclusions

We establish an effective strategy for developing nitrogen-doped SiOC-based ceramics by controlling molecular architectures through dendritic design. The synthesis of novel branched molecules enables tailored defect engineering, producing either highly defective materials with the D2 dendron or less defective structures with the D3 dendron. By adjusting the synthesis temperature, nitrogen incorporation can be directed both into the carbonaceous phase—enhancing graphitic-N through polymerization at 50 °C—and into the glassy network *via* Si–N bond formation during pyrolysis. This approach provides a powerful route to engineer ceramic materials with controlled nitrogen

functionalities, offering new opportunities for applications in electronics, catalysis, gas sensing, and energy storage.

Author contributions

J. R., M. A. M. and F. R.-M. conceived the idea. The research and experiments were planned by B. P.-R., A. M. R., J. R., M. A. M., and F. R.-M. Sample preparation was carried out by B. P.-R. and A. M. R, while structural characterization was performed by B. P.-R. Additionally, B. P.-R. conducted Raman measurements and microscopic strain characterization. The initial draft of the manuscript was written by B. P.-R., with contributions from M. A. M., J. R. and F. R.-M. All authors participated in the discussions and contributed to the final version of the manuscript. The work was supervised by M. A. M. and F. R.-M.

Conflicts of interest

There are no conflicts of interest to declare.

Data availability

The data supporting this article have been included as part of the supplementary information (SI). Supplementary information is available. See DOI: **https://doi.org/10.1039/d5ma00503e**.

In addition, the data that support the findings of this study are available from the corresponding author upon reasonable request.

Acknowledgements

References

1 E. Ionescu, H. J. Kleebe and R. Riedel, Silicon-Containing Polymer-Derived Ceramic Nanocomposites (PDC-NCs): Preparative Approaches and Properties, *Chem. Soc. Rev.*, 2012, **41**(15), 5032–5052, DOI: **10.1039/c2cs15319j**.

2 K. Xia, Y. Cheng, H. Zhang, F. Han, L. Duan and X. Liu, Highly Microporous Nitrogen-Doped Carbon Derived from Silicon Oxycarbide Ceramics for Supercapacitor Application, *J. Inorg. Organomet. Polym. Mater.*, 2023, **33**(7), 2023–2034, DOI: **10.1007/s10904-023-02627-7**.

3 S. B. Mujib, F. Ribot, C. Gervais and G. Singh, Self-Supporting Carbon-Rich SiOC Ceramic Electrodes for Lithium-Ion Batteries and Aqueous Supercapacitors, *RSC Adv.*, 2021, **11**(56), 35440–35454, DOI: **10.1039/d1ra05968h**.

4 R. Sujith, J. Gangadhar, M. Greenough, R. K. Bordia and D. K. Panda, A Review of Silicon Oxycarbide Ceramics as next Generation Anode Materials for Lithium-Ion Batteries and Other Electrochemical Applications, *J. Mater. Chem. A*, 2023, 20324–20348, DOI: **10.1039/d3ta01366a**.

5 G. Liu, J. Kaspar, L. M. Reinold, M. Graczyk-Zajac and R. Riedel, Electrochemical Performance of DVB-Modified SiOC and SiCN Polymer-Derived Negative Electrodes for Lithium-Ion Batteries, *Electrochim. Acta*, 2013, **106**, 101–108, DOI: **10.1016/j.electacta.2013.05.064**.

6 B. A. Karamoko, S. Dey, S. B. Mujib, J. Liu, W. Wang, J. Li, G. Singh, D. Voiry, C. Salameh, B. K. Yao and P. Miele, Polymer-Derived Silicon Oxycarbide/Graphene Oxide Porous Ceramic Monoliths Obtained from Pickering Emulsions: Application as Active Electrodes for Lithium-Ion Batteries, *Chem. Mater.*, 2024, **36**(7), 3138–3149, DOI: **10.1021/acs.chemmater.3c02502**.

7 R. Riedel, L. Toma, E. Janssen, J. Nuffer, T. Melz and H. Hanselka, Piezoresistive Effect in SiOC Ceramics for Integrated Pressure Sensors, *J. Am. Ceram. Soc.*, 2010, **93**(4), 920–924, DOI: **10.1111/j.1551-2916.2009.03496.x**.

8 M. Lu, H. Mei, S. Zhou, T. Zhao, L. Cheng and L. Zhang, Activation of Percolation Network in Structural-Strengthened Polymer-Derived Ceramic for Minor Deformation Detection, *Carbon*, 2021, **183**, 368–379, DOI: **10.1016/j.carbon.2021.07.023**.

9 M. Alejandra Mazo, I. Padilla, A. López-Delgado, A. Tamayo and J. Rubio, Silicon Oxycarbide and Silicon Oxycarbonitride Materials under Concentrated Solar Radiation, *Materials*, 2021, **14**(4), 1–19, DOI: **10.3390/ma14041013**.

10 M. Halasova, Z. Chlup, A. Strachota, M. Cerny and I. Dlouhy, Mechanical Response of Novel SiOC Glasses to High Temperature Exposition, *J. Eur. Ceram. Soc.*, 2012, **32**(16), 4489–4495, DOI: **10.1016/j.jeurceramsoc.2012.07.023**.

11 R. Bura, B. Kumar and R. M. Prasad, Polymer-Derived SiOC Ceramic Coating for Corrosion Protection, *Int. J. Appl. Ceram. Technol.*, 2024, **21**(2), 900–909, DOI: **10.1111/ijac.14588**.

12 F. Li, Y. Wang, W. Dang, Z. Xu, X. Zhang, B. Zhang, K. Zhao and Y. Tang, Effect of Curing Process and Pyrolysis Temperature on the Microstructure, Adhesion and Corrosion Resistance of PCS-Derived Coatings, *Ceram. Int.*, 2022, **48**(19), 28046–28058, DOI: **10.1016/j.ceramint.2022.06.110**.

13 P. Colombo, G. Mera, R. Riedel and G. D. Sorarù, Polymer-Derived Ceramics: 40 Years of Research and Innovation in Advanced Ceramics, *J. Am. Ceram. Soc.*, 2010, **93**(7), 1805–1837.

14 S. Trassl, G. Motz, E. Rössler and G. Ziegler, Characterisation of the Free-Carbon Phase in Precursor-Derived SiCN Ceramics, *J. Non-Cryst. Solids*, 2001, **293–295**, 261–267, DOI: **10.1016/S0022-3093(01)00678-0**.

15 S. Trassl, M. Puchinger, E. Rössler and G. Ziegler, Electrical Properties of Amorphous SiCxNyHz-Ceramics Derived from Polyvinylsilazane, *J. Eur. Ceram. Soc.*, 2003, **23**(5), 781–789, DOI: **10.1016/S0955-2219(02)00155-3**.

16 Q. Wen, Z. Yu and R. Riedel, The Fate and Role of in Situ Formed Carbon in Polymer-Derived Ceramics, *Prog. Mater. Sci.*, 2020, **109**, 100623, DOI: **10.1016/j.pmatsci.2019.100623**.

17 H. J. Kleebe and Y. D. Blum, SiOC Ceramic with High Excess Free Carbon, *J. Eur. Ceram. Soc.*, 2008, **28**(5), 1037–1042, DOI: **10.1016/j.jeurceramsoc.2007.09.024**.

18 H. Kleebe, H. Störmer, S. Trassl and G. Ziegler, Thermal Stability of SiCN Ceramics Studied by Spectroscopy and Electron Microscopy, *Appl. Organomet. Chem.*, 2001, **15**(10), 858–866.

19 M. Alejandra Mazo, A. Tamayo and J. Rubio, Stable Highly Porous Silicon Oxycarbide Glasses from Pre-Ceramic Hybrids, *J. Mater. Chem. A*, 2015, **3**(46), 23220–23229, DOI: **10.1039/c5ta05656j**.

20 M. A. Mazo, A. C. Caballero and J. Rubio, Further Insights into the Electrical and Thermal Properties of Carbon Enriched Silicon Oxycarbide Composites, *J. Alloys Compd.*, 2022, **889**, 17–21, DOI: **10.1016/j.jallcom.2021.161698**.

21 S. Kaur, G. Mera, R. Riedel and E. Ionescu, Effect of Boron Incorporation on the Phase Composition and High-Temperature Behavior of Polymer-Derived Silicon Carbide, *J. Eur. Ceram. Soc.*, 2016, **36**(4), 967–977, DOI: **10.1016/j.jeurceramsoc.2015.11.037**.

22 A. Klonczynski, G. Schneider, R. Riedel and R. Theissmann, Influence of Boron on the Microstructure of Polymer Derived SiCO Ceramics, *Adv. Eng. Mater.*, 2004, **6**(1–2), 64–68, DOI: **10.1002/adem.200300525**.

23 C. Schițco, C. Turdean-Ionescu, M. S. Bazarjani, C. W. Tai, D. Li, C. Fasel, W. Donner, J. Shen, R. Riedel, A. Gurlo and M. Edén, Silicon Oxycarbonitrides Synthesized by Ammonia-Assisted Thermolysis Route from Polymers: A Total X-Ray Scattering, Solid-State NMR, and TEM Structural Study, *J. Eur. Ceram. Soc.*, 2016, **36**(4), 979–989, DOI: **10.1016/j.jeurceramsoc.2015.11.004**.

24 E. G. Gillan, Synthesis of Nitrogen-Rich Carbon Nitride Networks from an Energetic Molecular Azide Precursor, *Chem. Mater.*, 2000, **12**(12), 3906–3912, DOI: **10.1021/cm000570y**.

25 H. Wang, T. Maiyalagan and X. Wang, Review on Recent Progress in Nitrogen-Doped Graphene: Synthesis, Characterization, and Its Potential Applications, *ACS Catal.*, 2012, **2**(5), 781–794, DOI: **10.1021/cs200652y**.

26 Q. Lv, N. Wang, W. Si, Z. Hou, X. Li, X. Wang, F. Zhao, Z. Yang, Y. Zhang and C. Huang, Pyridinic Nitrogen

Exclusively Doped Carbon Materials as Efficient Oxygen Reduction Electrocatalysts for Zn-Air Batteries, *Appl. Catal., B*, 2020, **261**, 118234, DOI: **10.1016/j.apcatb.2019.118234**.

27 R. Shibuya, T. Kondo and J. Nakamura, Active Sites in Nitrogen-Doped Carbon Materials for Oxygen Reduction Reaction, *Carbon-Based Met.-Free Catal. Des. Appl.*, 2018, **1**–2(6271), 227–249, DOI: **10.1002/9783527811458.vol1-ch8**.

28 L. Sun, C. Tian, Y. Fu, Y. Yang, J. Yin, L. Wang and H. Fu, Nitrogen-Doped Porous Graphitic Carbon as an Excellent Electrode Material for Advanced Supercapacitors, *Chem. – Eur. J.*, 2014, **20**(2), 564–574, DOI: **10.1002/chem.201303345**.

29 B. Pérez-Román, A. Merchán del Real, J. Rubio, M. A. Mazo and F. Rubio-Marcos, Innovative Strategies for Nitrogen-Incorporating Silicon Oxycarbide-Based Preceramic Polymer Synthesis, *Mater. Adv.*, 2024, **5**(5), 2040–2056, DOI: **10.1039/d3ma00898c**.

30 L. J. Print, J. J. Liggat, S. Moug, H. Seaton and D. C. Apperley, A Study of the Ceramicisation of Allylhydridopolycarbosilane by Thermal Volatilisation Analysis and Solid-State Nuclear Magnetic Resonance, *Silicon*, 2023, **15**(3), 1355–1379, DOI: **10.1007/s12633-022-02072-0**.

31 P. J. Larkin, M. P. Makowski, N. B. Colthup and L. A. Flood, Vibrational Analysis of Some Important Group Frequencies of Melamine Derivatives Containing Methoxymethyl, and Carbamate Substituents: Mechanical Coupling of Substituent Vibrations with Triazine Ring Modes, *Vib. Spectrosc.*, 1998, **17**(1), 53–72, DOI: **10.1016/S0924-2031(98)00015-0**.

32 R. Coustel, M. Haacké, V. Rouessac, E. André, S. Roualdès and A. Julbe, Vibrational Frequencies of Hydrogenated Silicon Carbonitride: A DFT Study, *Surf. Coat. Technol.*, 2017, **325**, 437–444, DOI: **10.1016/j.surfcoat.2017.06.017**.

33 S. P. Lee, N. Mellon, A. M. Shariff and J. M. Leveque, Adsorption of CO2 and Methane on Covalent Organic Polymer, *E3S Web Conf.*, 2018, **43**, 1–4, DOI: **10.1051/e3sconf/20184301001**.

34 A. Aldalbahi, B. Alotaibi and A. El-faham, Synthesis, Characterization of Sym-2,4,6-Trisubstituted-s-Triazine Derivatives and Their Effects on Flame Retardancy of Polypropylene Composites, *Processes*, 2020, **8**(581), 1–11, DOI: **10.3390/pr8050581**.

35 L. Stagi, D. Chiriu, M. Scholz, C. M. Carbonaro, R. Corpino, A. Porcheddu, S. Rajamaki, G. Cappellini, R. Cardia and P. C. Ricci, Vibrational and Optical Characterization of S-Triazine Derivatives, *Spectrochim. Acta, Part A*, 2017, **183**, 348–355, DOI: **10.1016/j.saa.2017.04.053**.

36 O. Alver and M. Senyel, Vibrational Spectroscopic and Conformational Studies of 1- (4- Pyridyl) Piperazine Vibrational Spectroscopic and Conformational Studies of 1-(4-Pyridyl) Piperazine, *Chem. Pap.*, 2010, **64**(4), 504–514, DOI: **10.2478/s11696-010-0021-y**.

37 S. Gunasekaran and B. Anita, Spectral Investigation and Normal Coordinate Analysis of Piperazine, *Indian J. Pure Appl. Phys.*, 2008, **46**(12), 833–838.

38 T. G. Torunoglu, K. Burak, Y. Erdem and S. Bahire Filiz, A New Multi-Hydroxyl Methacrylate Based Adsorbent for Boron Removal from Aqueous Solutions, *Sep. Sci. Technol.*, 2022, **57**(11), 1702–1713, DOI: **10.1080/01496395.2021.2006229**.

39 L. J. Print, J. J. Liggat, S. Moug, H. Seaton and D. C. Apperley, A Study of the Ceramicisation of Allylhydridopolycarbosilane by Thermal Volatilisation Analysis and Solid-State Nuclear Magnetic Resonance, *Silicon*, 2023, **15**(3), 1355–1379, DOI: **10.1007/s12633-022-02072-0**.

40 S. Kaur, R. Riedel and E. Ionescu, Pressureless Fabrication of Dense Monolithic SiC Ceramics from a Polycarbosilane, *J. Eur. Ceram. Soc.*, 2014, **34**(15), 3571–3578, DOI: **10.1016/j.jeurceramsoc.2014.05.002**.

41 H. Li, L. Zhang, L. Cheng, Y. Wang, Z. Yu, M. Huang, H. Tu and H. Xia, Effect of the Polycarbosilane Structure on Its Final Ceramic Yield, *J. Eur. Ceram. Soc.*, 2008, 887–891, DOI: **10.1016/j.jeurceramsoc.2007.07.020**.

42 R. Lee, *Carbosilanes: Reactions & Mechanisms of SMP-10 Pre-Ceramic Polymers*, 2009.

43 S. Kaur, G. Mônego, K. Rezwan and M. Wilhelm, Synthesis of Porous Ni/SiC(O)-Based Nanocomposites: Effect of Nickel Acetylacetonate and Poly(Ethylene Glycol) Methacrylate Modification on Specific Surface Area and Porosity, *Adv. Eng. Mater.*, 2020, **22**, 1901036, DOI: **10.1002/adem.201901036**.

44 Q. Wen, Y. Xu, B. Xu, C. Fasel, O. Guillon, Z. Y. Gerd Buntkowsky, R. Riedela and E. Ionescu, Single-Source-Precursor Synthesis of Dense SiC/HfC$_x$N$_{1-x}$-Based Ultrahigh-Temperature Ceramic Nanocomposites, *Nanoscale*, 2014, **6**, 13678–13689, DOI: **10.1039/c4nr03376k**.

45 C. Sugie, A. Navrotsky, S. Lauterbach, H. J. Kleebe and G. Mera, Structure and Thermodynamics of Silicon Oxycarbide Polymer-Derived Ceramics with and without Mixed-Bonding, *Materials*, 2021, **14**(15), 4075, DOI: **10.3390/ma14154075**.

46 D. De Sousa Meneses, M. Eckes, L. Del Campo, C. N. Santos, Y. Vaills and P. Echegut, Investigation of Medium Range Order in Silicate Glasses by Infrared Spectroscopy, *Vib. Spectrosc.*, 2013, **65**, 50–57, DOI: **10.1016/j.vibspec.2012.11.015**.

47 L. Xu, R. Liu, F. Wang, S. Yan, X. Shi and J. Yang, Preparation of Triazine Containing Porous Organic Polymer for High Performance Supercapacitor Applications, *RSC Adv.*, 2019, **9**(3), 1586–1590, DOI: **10.1039/C8RA09099H**.

48 S. Maldonado, S. Morin and K. J. Stevenson, Structure, Composition, and Chemical Reactivity of Carbon Nanotubes by Selective Nitrogen Doping, *Carbon*, 2006, **44**(8), 1429–1437, DOI: **10.1016/j.carbon.2005.11.027**.

49 A. Mirzaei, S. P. Bharath, J. Y. Kim, K. K. Pawar, H. W. Kim and S. S. Kim, N-Doped Graphene and Its Derivatives as Resistive Gas Sensors: An Overview, *Chemosensors*, 2023, **11**(6), 334, DOI: **10.3390/chemosensors11060334**.

50 Y. Jiang, S. Chowdhury and R. Balasubramanian, New Insights into the Role of Nitrogen-Bonding Configurations in Enhancing the Photocatalytic Activity of Nitrogen-Doped Graphene Aerogels, *J. Colloid Interface Sci.*, 2019, **534**, 574–585, DOI: **10.1016/j.jcis.2018.09.064**.

51 J. Li, W. Y. Zan, H. Kang, Z. Dong, X. Zhang, Y. Lin, Y. W. Mu, F. Zhang, X. M. Zhang and J. Gu, Graphitic-N Highly Doped Graphene-like Carbon: A Superior Metal-Free Catalyst for Efficient Reduction of CO2, *Appl. Catal., B*, 2021, **298**, 120510, DOI: **10.1016/j.apcatb.2021.120510**.

52 J. S. S. Neto and G. Zeni, Transition Metal-Catalyzed and Metal-Free Cyclization Reactions of Alkynes with Nitrogen-Containing Substrates: Synthesis of Pyrrole Derivatives, *ChemCatChem*, 2020, **12**(13), 3335–3408, DOI: **10.1002/cctc.201902325**.

53 I. V. Efimov, D. I. Zhilyaev, L. N. Kulikova and L. G. Voskressensky, Cycloaddition Reactions of Enamines, *Eur. J. Org. Chem.*, 2023, **26**, e202201450, DOI: **10.1002/ejoc.202201450**.

54 J. Corthout, L. Pieters, M. Claeys, S. Geerts, D. V. Berghe and A. Vlietinck, *Enamines: General and Theoretical Aspects*, 1994, vol. 60.

55 H. Gao, S. Wang, W. C. M. Cheong, K. Wang, H. Xu, A. Huang, J. Ma, J. Li, W. F. A. Ip, K. San Hui, D. A. Dinh, X. Fan, F. Bin, F. Chen and K. N. Hui, Topological Defect and Sp3/Sp2 Carbon Interface Derived from ZIF-8 with Linker Vacancies for Oxygen Reduction Reaction, *Carbon*, 2023, **203**(2022), 76–87, DOI: **10.1016/j.carbon.2022.10.030**.

56 G. J. Leonel, X. Guo, G. Singh, C. Gervais and A. Navrotsky, Energetics and Structure of SiC(N)(O) Polymer-Derived Ceramics, *J. Am. Ceram. Soc.*, 2023, 5086–5101, DOI: **10.1111/jace.19153**.

57 Y. Feng, N. Feng, Y. Wei and Y. Bai, Preparation and Improved Electrochemical Performance of SiCN-Graphene Composite Derived from Poly(Silylcarbondiimide) as Li-Ion Battery Anode, *J. Mater. Chem. A*, 2014, **2**(12), 4168–4177, DOI: **10.1039/c3ta14441k**.

58 C. Gérardin, F. Taulelle and D. Bahloul, Pyrolysis Chemistry of Polysilazane Precursors to Silicon Carbonitride: Part 2. – Solid-State NMR of the Pyrolytic Residues, *J. Mater. Chem.*, 1997, **7**(1), 117–126, DOI: **10.1039/a603181a**.

59 C. Gervais, Solid-State NMR Applied to Si-Based Polymer Derived Ceramics: A Review, *Open Ceram.*, 2023, **15**, 100376, DOI: **10.1016/j.oceram.2023.100376**.

60 N. Brodie, J.-P. Majoral and J.-P. Disson, An NMR Study of the Step by Step Pyrolysis of a Polysilazane Precursor of Silicon Nitride, *Inorg. Chem.*, 1993, **32**, 4646–4649.

61 H. W. Kim, H. Park, J. S. Roh, J. E. Shin, T. H. Lee, L. Zhang, Y. H. Cho, H. W. Yoon, V. J. Bukas, J. Guo, H. B. Park, T. H. Han and B. D. McCloskey, Carbon Defect Characterization of Nitrogen-Doped Reduced Graphene Oxide Electrocatalysts for the Two-Electron Oxygen Reduction Reaction, *Chem. Mater.*, 2019, **31**(11), 3967–3973, DOI: **10.1021/acs.chemmater.9b00210**.

62 F. Tuinstra and J. L. Koenig, Raman Spectrum of Graphite, *J. Chem. Phys.*, 1970, **53**(3), 1126–1130, DOI: **10.1063/1.1674108**.

63 A. Merlen; J. G. Buijnsters and C. Pardanaud, *A Guide to and Review of the Use of Multiwavelength Raman Spectroscopy for Characterizing Defective Aromatic Carbon Solids: From Graphene to Amorphous Carbons*, 2017, vol. 7, DOI: **10.3390/coatings7100153**.

64 A. C. Ferrari and J. Robertson, Interpretation of Raman Spectra of Disordered and Amorphous Carbon, *Phys. Rev. B:Condens. Matter Mater. Phys.*, 2000, **61**(20), 14095–14107, DOI: **10.1007/BF02543692**.

65 R. Peña-Alonso, G. D. Sorarù and R. Raj, Preparation of Ultrathin-Walled Carbon-Based Nanoporous Structures by Etching Pseudo-Amorphous Silicon Oxycarbide Ceramics, *J. Am. Ceram. Soc.*, 2006, **89**(8), 2473–2480, DOI: **10.1111/j.1551-2916.2006.01117.x**.

66 T. Sharifi, F. Nitze, H. R. Barzegar, C.-W. Tai, M. Mazurkiewicz, A. Malolepszy, L. Stobinski and T. Wågberg, Nitrogen Doped Multi Walled Carbon Nanotubes Produced by CVD-Correlating XPS and Raman Spectroscopy for the Study of Nitrogen Inclusion, *Carbon*, 2012, **50**(10), 3535–3541, DOI: **10.1016/j.carbon.2012.03.022**.

67 A. Eckmann, A. Felten, A. Mishchenko, L. Britnell, R. Krupke, K. S. Novoselov and C. Casiraghi, Probing the Nature of Defects in Graphene by Raman Spectroscopy, *Nano Lett.*, 2012, **12**(8), 3925–3930, DOI: **10.1021/nl300901a**.

68 A. Sadezky, H. Muckenhuber, H. Grothe, R. Niessner and U. Pöschl, Raman Microspectroscopy of Soot and Related Carbonaceous Materials: Spectral Analysis and Structural Information, *Carbon*, 2005, **43**(8), 1731–1742, DOI: **10.1016/j.carbon.2005.02.018**.

69 V. L. Nguyen, N. B. Laidani and G. D. Sorarù, N-Doped Polymer-Derived Si(N)OC: The Role of the N-Containing Precursor, *J. Mater. Res.*, 2015, **30**(6), 770–781, DOI: **10.1557/jmr.2015.44**.